TWO-DIMENSIONAL ELECTRON SYSTEM ON A CURVED SURFACE WITH A

CONSTANT RADIUS

NUT PRAMJORN

A Thesis Submitted to the Graduate School of Naresuan University

in Partial Fulfillment of the Requirements

for the Doctor of Philosophy in Physics - Type 2.2

2022

TWO-DIMENSIONAL ELECTRON SYSTEM ON A CURVED SURFACE WITH A

CONSTANT RADIUS

NUT PRAMJORN

A Thesis Submitted to the Graduate School of Naresuan University

in Partial Fulfillment of the Requirements

for the Doctor of Philosophy in Physics - Type 2.2

2022

Thesis entitled "Two-dimensional electron system on a curved surface with a constant radius"

By Nut Pramjorn

has been approved by the Graduate School as partial fulfillment of the requirements

for the Doctor of Philosophy in Physics - Type 2.2 of Naresuan University

Oral Defense Committee

-- Chair

(Assistant Professor Pichitchai Pimpang, Ph.D.)

-- Advisor

(Associate Professor Attapon Amthong, Ph.D.)

-- Internal Examiner

(Assistant Professor Aek Jantayod, Ph.D.)

-- Internal Examiner

(Assistant Professor Sasipohn Prasertpalichat, Ph.D.)

-- Internal Examiner

(Assistant Professor Jaru Jutimoosik, Ph.D.)

Approved

(Associate Professor Krongkarn Chootip, Ph.D.)

Dean of the Graduate School

ABSTRACT

Two topics of two-dimensional electron systems on a curved surface with a constant radius are studied in this dissertation: the binding energies and impurity states of a single donor and the oscillator strength property in the system in the presence of an electric field. For both, we solve the Schrödinger equation for energy levels and eigenfunctions by using a finite difference approach within the scope of the effective-mass approximation. Then those results are brought to calculate the binding energies and the oscillator strength. The impacts of donor positions, curvature, and system size on the binding energies are discussed. We observe that when the radius of such a system is less than the effective Bohr radius, the binding energy increase considerably. Additionally, by changing the direction of an external electric field, it is possible to efficiently manipulate the values of a donor's binding energies at certain places. The effect of tilt angles can enhance the oscillator strength along the x-direction, and the electric field on the -x-direction considerably upgrades the oscillator strength along the y-direction, especially when the curvature is numerous.

ACKNOWLEDGEMENTS

Nut Pramjorn

TABLE OF CONTENTS

CHAPTER 1 INTRODUCTION

Electronic devices related to dopants are getting much attention nowadays [1]. Donor impurities generate coulomb potential energy that significantly affects device features and increases capability. For instance, either random or normal distribution of the dopants in the channel can establish the threshold voltage in the field-effect transistor (FET) [1, 2]. In addition, the Coulomb potential energy from a dopant can also produce source and drain current extremums below the conduction band in the Fin field-effect transistor (FinFET) [3, 4]. Another exciting application is quantum bits that store information and perform calculations in quantum computers. Particles trapped in double potential donor wells can be used as qubits in quantum computing [5-7]. Furthermore, the effect of donor dopants is related to phenomena in optical devices such as microdisks where donor-bound excitons experimentally reduce the threshold lasing [8]. The multiple advantages of adding donor impurities have resulted in many studies of binding energy in diverse kinds of such low-dimensional systems [9-13].

Spatial confinement, impurity location, and external field influence the donor binding energy in nanostructures. When a donor is placed in the center of both finite and core-shell spherical quantum dots, the binding energy gradually declines while expanding the confinement area [14-17]. Nevertheless, it fluctuates in multilayered quantum dots [18] because an electron can tunnel through a barrier potential. External influences such as a magnetic field and an electric field also control the binding energy. A magnetic field can produce an additional potential that attracts an electron wavefunction into the sphere's center. In contrast, an electric field pushes an electron probability density away from a donor, decreasing the binding energy.

In addition, there is a similar investigation on the quantum wires as well [19-22]. A magnetic field can enhance the binding energy in a coaxial quantum well wire when a donor impurity is localized in the inner wire, as previously described by Aktas et al. [19]. However, the binding energy is reduced when the impurity is doped to the outer wire. Moreover, the donor location can affect the electric field's impact on the binding energy, and this result became more apparent when the dopant was positioned in the outer wire.

Another research from Tangarife and Duque investigated the binding energy on hydrostatic pressure in a double quantum-well wire [20]. They controlled the electron coupling on both left and right wires by adjusting the pressure. As a result, an electric field with hydrostatic pressure handle electron distribution and binding energy value more efficiently.

For the quantum potential well, there are recently published works. Hu et al. studied the effects of different potential wells, including rectangular, V-shaped, and parabolic potential wells, on the binding energy [23]. The results showed that the location of a dopant has the most apparent impact on the binding energy in the V-shaped potential. However, in the rectangular potential, the width of the well has the most significant effect on the binding energy. The electric field and magnetic field are comparable effects on the binding energy of three quantum wells. Kalpana et al. investigated the binding energy in double wells system with a donor impurity created from a dilute magnetic semiconductor [24]. The research revealed that the binding energy is still high even though a dopant is localized in the magnetic material wall, whose height can be adjusted by an external magnetic field. Lastly, Vartanian et al. considered the binding energy in a near-surface quantum well [25]. They found that the image charge and a dopant can influence the binding energy effectively, giving them positive energy. The binding energy drastically decreases if a dopant is near a vacuum.

The famous structure in the present is a curved two-dimensional electron system (2DES) which confines electrons to only move on the surface. A spherical surface [26, 27] and a rolled-up multilayer [28-33] are examples of structural surfaces studied for many years. Mainly, roll-up multilayer, in which we are interested, is generally produced by removing a substance layer. As a result, semiconducting layers roll by their strain effect. Applications of a curved 2DES are optical resonators [34, 35], microtube refractometers [36], and fluidic devices [37, 38]. Although the system has been studied until it can be applied in the real world, research about a donor in a curved 2DES is obscure. Since modern technology can precisely introduce an impurity to the system, studying the influences of a donor is necessary.

The light absorption of structures has been one of the optical properties that have been studied for many decades. There are many physical quantities that can be linked to absorbance. One popular quantity is the oscillator strength, which is a quantity that represents the probability of an electron being stimulated to higher energy levels [39, 40]. For example, Wu et al. studied the effect of an external electric field on the absorbance of a shallow InAs/InP quantum wire structure [41]. They discovered that an angle of an external electric field can control the sensitivity and the wavelength of incident light that the structure will be responsive to. Özmen et al. studied the oscillator strength and absorption coefficient of spherical quantum dot structures with a donor at the center of the dot [42]. They discovered that the donor greatly affected the optical properties. It will greatly reduce the oscillator strength, especially for a large dot. Moreover, the donor also results in the quantum dot absorbing incident light at higher energy levels.

This dissertation studies various consequences of doping a donor in a curved surface electron system in a rolled-up form [43, 44]. The system is a model of GaAs and $Al_{0.33}Ga_{0.67}As$ layers with a fixed curvature. The positivity due to a dopant atom creates the Coulomb force that attracts free electrons on the surface. We examine the system's energies in the case of a flat and large area to the two-dimensional electron system to confirm our calculation results [45, 46]. The researcher begins to study the effect of the curvature on the first two energy levels of the system. Then the donor is repositioned to observe the unpredictable binding energies of the system. Moreover, after applying an external electric field, it has several unforeseen impacts on the binding energies. The electron distribution in the absence of a dopant can help explain the various effects. In another section of this dissertation, the researcher investigates the effect of structure and electric field on the oscillator strength of the curved surface system without an impurity. This research is only interested in the transition between the ground state and the first excited state.

CHAPTER 2 BACKGROUND KNOWLEDGE

Two-dimensional electron system

The term "two-dimensional electron system" refers to two-dimensional electron gas systems in general. It is a solid-state physics scientific model, an electron gas that distributes in two dimensions but is firmly restricted in the third. Because of the tight confinement, energy levels are quantized in the third direction, which most studies can ignore. As a result, the electrons appear to be a two-dimensional sheet embedded in a three-dimension, such as an interface between thin silicon and insulating silicon dioxide layer or the interface between GaAs and AlGaAs. This action can produce a system of electrons on the surface that would be further confined in other directions, such as by magnetic or electric fields. This research focuses on the electrons in GaAs/GaAlAs; therefore, a brief overview of fabrication will be provided.

A 2DEG can be created, with the additional benefit of being generated at a crystalline GaAs/AlGaAs heterointerface. Its energy band gap allows the carriers to be constrained to a 2D plane. While GaAs (5.653 Å) and AlAs (5.660 Å) have identical lattice spacing, the band gap is vastly different. We can amplify a wide range of band gaps at ambient temperature if we adjust a concentration of Ga that would be doped in AlGaAs. It is feasible to design the band gap by generating a sequence of layers with varied characteristics in heterojunction devices using techniques such as molecular beam epitaxy (MBE) [47, 48].

Discontinuities in the conduction and valence bands occur when a layer of AlGaAs is formed on top of a layer of GaAs. It is acceptable to place donors in an AlGaAs layer some distance apart from the interface where the 2DEG is produced using a process known as modulation doping [49-51]. Dopant ions are left behind when electrons from these donors diffuse into the GaAs region with a narrow band gap. Once an n-type doped layer is used, the Fermi energy in that layer is pushed toward the conduction band. Since the AlGaAs layer expresses the positive charge, the bands in the interface bend upward to balance the internal electric field. Therefore, carriers can

be trapped and formed into a surface with a triangle quantum-well in the conduction band occurred, as shown in Figure 1.
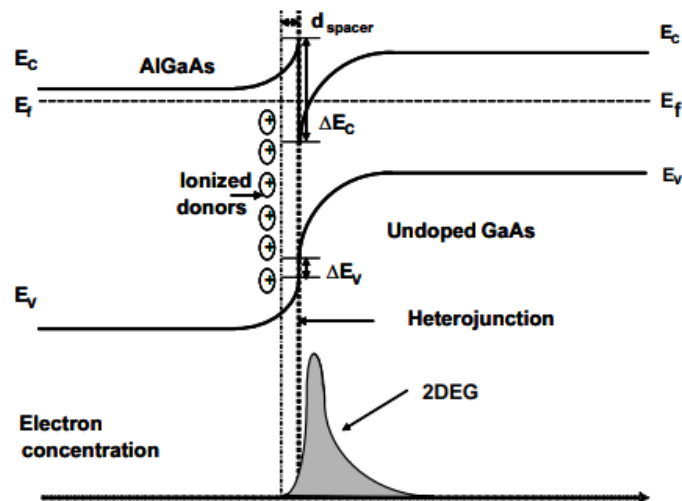
Figure 1. A band diagram is formed by a GaAs/AlGaAs heterostructure with an n-type doping layer and an inherent AlGaAs gap layer [52]

The development of such a system can lead to the research of electron processes in two dimensions, as well as applications in the manufacture of various electronic devices. In this research, we will investigate the electron system which is curved in two dimensions and explore the traits that result from those systems.

Doped semiconductors

Doping impurities into crystals is essential today because intrinsic semiconductors typically have low electrical conductivity. However, when the impurities were doped, it was able to stimulate the conductivity of the semiconductor. For example, silicon and germanium crystals are group four elements on the periodic table. It is found that the bonds of each atom share valence electrons with all four surrounding atoms, and there are no electrons that have mobility within the crystal. As a result, the electrical conductivity is unpleasant. Nevertheless, suppose the atoms of group three and group five elements are doped into the crystal. In that case, free electrons or holes are formed

in the atomic dopant region, which results in better conductivity. The addition of atoms can be divided into two types: [53]

The first type involves doping an element with more valence electrons than one of the original atoms in some places in the original crystal. In Figure 2, when doped to silicon crystals, phosphorus or arsenic is found to have an unpaired electron, which is excited in the conduction band of silicon and can move to different positions of the crystal, causing electricity to occur. Atoms doped to a semiconductor to form free electrons are called "donors," and the addition of atoms in such a way is known as "n-doped."
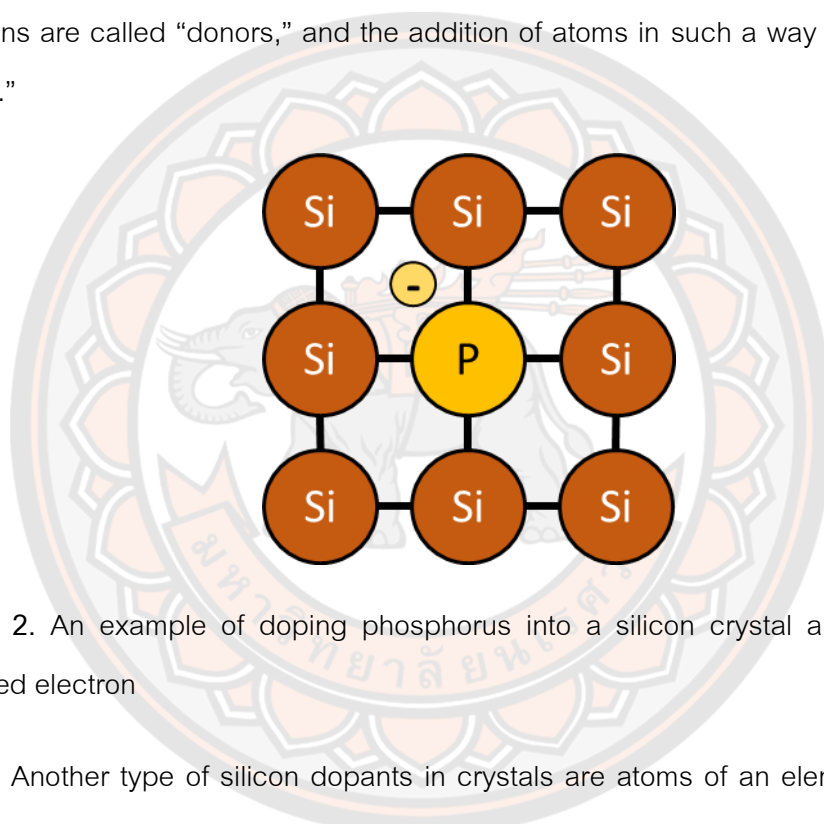
Figure 2. An example of doping phosphorus into a silicon crystal and leaving one unpaired electron

Another type of silicon dopants in crystals are atoms of an element with fewer valence electrons than one of the atoms in the original crystal, such as aluminum or gallium. In Figure 3, an example of doping aluminum, a group of three elements to silicon crystals, shows that aluminum can only share three electrons with silicon. Thus, electron holes occur around aluminum, and the movement of these positive holes can cause an electric current similar to the flow of electrons. These atoms added to a crystal are called "acceptors." This process is called "p-doped."
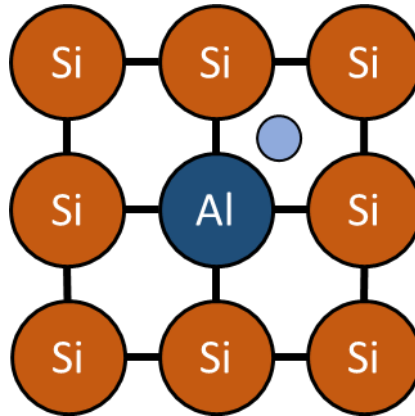
Figure 3. An example of doping aluminium into a silicon crystal and leaving hole

The concentration of the impurity atom can be determined to change the properties of the original crystal. In this dissertation, GaAlAs/GaAs crystals were to be doped in the process of n-doped by using silicon atoms to induce electrons in the conduction band and move them to the junction between GaAlAs and GaAs. It creates a two-dimensional electron system following the guidelines of the previous section. Furthermore, the donor is doped near the junction, causing the Coulomb potential in the vicinity of a donor atom.

Analytic solution of two-dimensional Hydrogen atom

A two-dimensional hydrogen atomic system is analogous to placing donor dopants into a two-dimensional surface. If a two-dimensional surface is sufficiently large, the resulting energy level approaches the two-dimensional energy level of the hydrogen atom. The results of this system can be compared to the numerical calculations employed in this study to determine whether the results are valid and consistent. The two-dimensional hydrogen atomic system begins with the interaction of protons and electrons, as well as the three-dimensional system. The electron's potential energy $V(r)$ is defined as

$$V(r) = \frac{Ze^2}{r}.$$ (2.1)

$Z = \dfrac{1}{4\pi\varepsilon_0}$, where ε_0 is the vacuum permittivity. r indicates the distance between the proton and the electron. The time independent Schrödinger equation of the system in polar coordinate is

$$\left[-\frac{\hbar^2}{2\mu}\left(\frac{\partial^2}{\partial r^2} + \frac{1}{r}\frac{\partial}{\partial r} + \frac{1}{r^2}\frac{\partial^2}{\partial \phi^2} \right) - \frac{Ze^2}{r} \right]\Psi(r,\phi) = E\Psi(r,\phi), \qquad (2.2)$$

where μ, Ψ and E denote the electron's effective mass, the wavefunction and the energy respectively. The wavefunction can be separated to $R(r)$ and $\Phi(\phi)$ as

$$\Psi(r,\phi) = R(r)\Phi(\phi). \qquad (2.3)$$

By substituting equation (2.3) to equation (2.2),

$$\left[-\frac{\hbar^2}{2\mu}\left(\frac{\partial^2}{\partial r^2} + \frac{1}{r}\frac{\partial}{\partial r} + \frac{1}{r^2}\frac{\partial^2}{\partial \phi^2} \right) - \frac{Ze^2}{r} \right]R(r)\Phi(\phi) = ER(r)\Phi(\phi). \qquad (2.4)$$

Equation (2.4) can be rewritten as

$$r^2\frac{R''(r)}{R(r)} + r\frac{R'(r)}{R(r)} + \frac{2\mu}{\hbar^2}r^2\left(\frac{Ze^2}{r} + E \right) = -\frac{\Phi''(\phi)}{\Phi(\phi)}. \qquad (2.5)$$

By defining $-\dfrac{\Phi''(\phi)}{\Phi(\phi)} \equiv \ell^2$, where ℓ is a constant value, the solution of $\Phi(\phi)$ is

$$\Phi(\phi) = C_\phi e^{i|\ell|\phi}, \qquad (2.6)$$

where C_ϕ is a normalized constant. From equation (2.6), equation (2.5) can be rewritten as

$$r^2\frac{R''(r)}{R(r)} + r\frac{R'(r)}{R(r)} + \frac{2\mu}{\hbar^2}r^2\left(\frac{Ze^2}{r} + E \right) = \ell^2. \qquad (2.7)$$

Equation (2.7) can be simplified as

$$R''(r) + \frac{1}{r}R'(r) + \left[\frac{2\mu}{\hbar^2}\left(\frac{Ze^2}{r} + E \right) - \frac{\ell^2}{r^2} \right]R(r) = 0. \qquad (2.8)$$

Then redefine r as a function of x, that is, $r \equiv \dfrac{N\hbar^2}{2\mu Ze^2}x$, and define $\beta_N \equiv \dfrac{2\mu Ze^2}{N\hbar^2}$, where N is a constant value. The result of equation (2.8) is

$$\beta_N^2 R''(x) + \frac{\beta_N^2}{x}R'(x) + \left[\frac{2\mu}{\hbar^2}\left(\beta_N\frac{Ze^2}{x} + E \right) - \beta_N^2\frac{\ell^2}{x^2} \right]R(x) = 0. \qquad (2.9)$$

Equation (2.9) can be simplified by dividing both sides of equation (2.9) by β_N^2,

$$R''(x) + \frac{1}{x}R'(x) + \left[\frac{N}{x} + \frac{\hbar^2 N^2 E}{2\mu Z^2 e^4} - \frac{\ell^2}{x^2}\right]R(x) = 0. \tag{2.10}$$

By defining $E \equiv -\frac{Z^2}{2N^2}\left(\frac{\mu e^4}{\hbar^2}\right)$, equation (2.10) becomes

$$R''(x) + \frac{1}{x}R'(x) + \left[\frac{N}{x} - \frac{1}{4} - \frac{\ell^2}{x^2}\right]R(x) = 0. \tag{2.11}$$

Then equation (2.11) is considered that x converges to zero, meaning r also approaches zero. Equation (2.11) in the following specific case is

$$R''(x) + \frac{1}{x}R'(x) - \frac{\ell^2}{x^2}R(x) = 0. \tag{2.12}$$

The solution of equation (2.12) is solved by distributing $R(x)$ into power series. Consequently, the result which is acquired is

$$R(x) = C_R^1 x^{|\ell|}, \tag{2.13}$$

where C_R^1 is normalized constant. Another extreme case is x diverge, meaning r is enormous. Equation (2.11) can be simplified as

$$R''(x) - \frac{1}{4}R(x) = 0, \tag{2.14}$$

The solution of equation (2.14) is simply solved analytically which is

$$R(x) = C_R^2 e^{-x/2}. \tag{2.15}$$

C_R^2 is normalized constant. Eventually, equation (2.13) and (2.15) are combined to yield the appropriate solution as follow

$$R(x) = x^{|\ell|} e^{-x/2} G(x), \tag{2.16}$$

where $G(x)$ is an arbitrary function which is corresponding to the expression. By substituting equation (2.16) to (2.11), we obtain

$$xG''(x) + \left(2|\ell| - x + 1\right)G'(x) - \left(-N + |\ell| + \frac{1}{2}\right)G(x) = 0. \tag{2.17}$$

Equation (2.17) is a form of Kummer's equation, whose the solution is a confluent hypergeometric function F [54, 55],

$$G(x) = {}_1F_1\left(-N + |\ell| + \frac{1}{2}, 2|\ell| + 1, x\right). \tag{2.18}$$

This answer is valid when $-N+|\ell|+\dfrac{1}{2}\le 0$, so $N=\dfrac{1}{2},\dfrac{3}{2},\dfrac{5}{2},\dots$. n is defined for indicating energy levels, which are integers, therefore the energy levels E are rewritten as

$$E = -\frac{Z}{2\left(n-\dfrac{1}{2}\right)^2}\frac{\mu e^4}{\hbar^2} \tag{2.19}$$

with $n=N+\dfrac{1}{2}=1,2,3,\dots$. From equation (2.18), the general solution of $R(x)$ is

$$R(x) = Px^{|\ell|}e^{-x/2}\,_1F_1\left(-n+|\ell|+1,2|\ell|+1,x\right), \tag{2.20}$$

where P is a normalized constant. If $R(x)$ is converted to the function of distance r, it becomes

$$R(r) = P\left(\beta_N r\right)^{|\ell|}e^{-\beta_N r/2}\,_1F_1\left(-n+|\ell|+1,2|\ell|+1,\beta_N r\right). \tag{2.21}$$

The part of confluent hypergeometric function can be expanded in terms of Laguerre polynomials as follow

$$_1F_1\left(-n+|\ell|+1,2|\ell|+1,\beta_N r\right) = \frac{(2|\ell|)!(n-|\ell|-1)!}{(n+|\ell|-1)!}L_{n-|\ell|-1}^{2|\ell|}(\beta_N r), \tag{2.22}$$

where $L_{n-|\ell|-1}^{2|\ell|}(\beta_N r)$ denotes Laguerre polynomials. By substituting equation (2.22) to equation (2.21), $R(r)$ can be rewritten in terms of Laguerre polynomials as follow

$$R(r) = P\left(\beta_N r\right)^{|\ell|}e^{-\beta_N r/2}\frac{(2|\ell|)!(n-|\ell|-1)!}{(n+|\ell|-1)!}L_{n-|\ell|-1}^{2|\ell|}(\beta_N r) \tag{2.23}$$

From equation (2.23), if $R(r)$ is normalized, we acquire

$$P = \frac{\beta_N}{(2|\ell|)!}\left[\frac{(n+|\ell|-1)!}{(2n-1)(n-|\ell|-1)!}\right]^{1/2} \tag{2.24}$$

Finally, the analytic solution of $R(r)$ part is

$$R(r) = \frac{\beta_N}{(2|\ell|)!}\left[\frac{(n+|\ell|-1)!}{(2n-1)(n-|\ell|-1)!}\right]^{1/2}(\beta_N r)^{|\ell|}e^{-\beta_N r/2}\,_1F_1\left(-N+|\ell|+\frac{1}{2},2|\ell|+1,\beta_N r\right),$$

$$\tag{2.25}$$

corresponding to the previous research about two-dimensional hydrogen atom [45].

Oscillator strength in a flat surface system

Oscillator strength is a dimensionless quantity that indicates the probability of electron transition between two arbitrary states from the incident light [39, 40]. If we consider a curved surface system, the oscillator strength f_{nm} along the ϕ-direction between the state $|n\rangle$ and state $|m\rangle$ are defined as

$$f_{nm} = \frac{2\mu}{\hbar^2}(E_m - E_n)|\langle m|\vec{r}|n\rangle|^2,$$ (2.26)

where μ is an electron's effective mass and $\hbar$ is the reduced Planck constant. E_n and E_m are energy levels of the state $|n\rangle$ and state $|m\rangle$, respectively. The operator $\vec{r}$ is the coordinate corresponding to the polarization of the incident light. For example, if a given polarization of the light is in the x-direction, $\vec{r}$ becomes a position operator $\bar{x}$ in the Cartesian coordinate. $\langle m|\vec{r}|n\rangle$, called the transition dipole moment, determines the coupling between two states and how strong the system will interact with the incident light. Since the quantity of oscillator strength is proportional to the intersubband transition rate from Fermi's golden rule, [41] the oscillator strength can also be used as another measurement for absorption intensity in an optical system.

The Thomas-Reiche-Kuhn (TRK) sum rule helps us confirm that the oscillator strength is implemented correctly. For instance, the derivation of the sum rule along the x-direction begins with two commutation relations,

$$[\hat{e}_x p_x, \hat{e}_x x] = \frac{\hbar}{i}$$ (2.27)

and

$$[H, \hat{e}_x x] = \hat{e}_x \frac{\hbar}{\mu i} p_x.$$ (2.28)

$\hat{e}_x$ is the unit vector of the Cartesian coordinate along the x-axis. The operator p_x is the momentum along the x-direction. In a two-dimensional flat surface, the Hamiltonian can be written as $H = -\frac{\hbar^2}{2\mu}\left(\frac{\partial^2}{\partial x^2} + \frac{\partial^2}{\partial y^2}\right) + V(x) + V(y)$ where μ are the electron's effective mass. $V(x)$ and $V(y)$ are the arbitrary potentials of the system. For a simplification, $V(x)$ and $V(y)$ are zero values on the surface region and infinite on the

otherwise because of the geometric confinement. If a commutator $\left[\hat{e}_x\hat{p}_x,\hat{e}_x x\right]$ in equation (2.27) is calculated and inserted a complete set of states, we will obtain

$$\left\langle n\left|\hat{e}_x p_x\cdot\hat{e}_x x-\hat{e}_x x\cdot\hat{e}_x p_x\right|n\right\rangle=\sum_m\left(\left\langle n\left|\hat{e}_x p_x\right|m\right\rangle\cdot\left\langle m\left|\hat{e}_x x\right|n\right\rangle-\left\langle n\left|\hat{e}_x x\right|m\right\rangle\cdot\left\langle m\left|\hat{e}_x p_x\right|n\right\rangle\right).$$

(2.29)

$\left|n\right\rangle$ and $\left|m\right\rangle$ are two arbitrary quantum states which are orthogonal. After the calculation, the relation in equation (2.28) can be written as

$$\left\langle n\left|\hat{e}_x p_x\right|m\right\rangle=\frac{\mu i}{\hbar}\left(E_n-E_m\right)\left\langle n\left|\hat{e}_x x\right|m\right\rangle$$

(2.30)

and

$$\left\langle m\left|\hat{e}_x p_x\right|n\right\rangle=\frac{\mu i}{\hbar}\left(E_m-E_n\right)\left\langle m\left|\hat{e}_x x\right|n\right\rangle.$$

(2.31)

By substituting equation (2.30) and (2.31) into equation (2.29), the desired result is

$$\frac{\hbar^2}{2\mu}=\sum_m\left(E_m-E_n\right)\left|\left\langle m\left|\hat{e}_x x\right|n\right\rangle\right|^2$$

(2.32)

Equation (2.32) leads to the important condition of the oscillator strength along the x-direction,

$$1=\frac{2\mu}{\hbar^2}\sum_m\left(E_m-E_n\right)\left|\left\langle m\left|\hat{e}_x x\right|n\right\rangle\right|^2.$$

(2.33)

Furthermore, If the derivation of the y-direction uses the similar implementation, the sum rule of the oscillator strength along the y-direction becomes

$$1=\frac{2\mu}{\hbar^2}\sum_m\left(E_m-E_n\right)\left|\left\langle m\left|\hat{e}_y y\right|n\right\rangle\right|^2.$$

(2.34)

y and $\hat{e}_y$ are the position operator in the y-direction and the unit vector of the Cartesian coordinate along the y-axis, respectively.

CHAPTER 3 METHODOLOGY AND CALCULATION

A curved surface electron system

Firstly, a curved surface electron system in the absence of impurity. As a result, we consider a rectangular two-dimensional plane with length L and width W that is rolled and has a constant radius R, as shown in Figure 4. The angle ϕ and the depth z are utilized to identify the positions on the cylindrical surface. The relation between radius R and width W is $W = R(\phi_{max} - \phi_{min})$ where ϕ_{min} and ϕ_{max} indicate the edge of a curved surface in the ϕ-axis. s is a coordinate, relating with R as $s = R\phi$, along the curve of a surface. Within the effective mass approximation, we can derive the energy levels and wavefunctions of the system's electrons from the Schrödinger equation
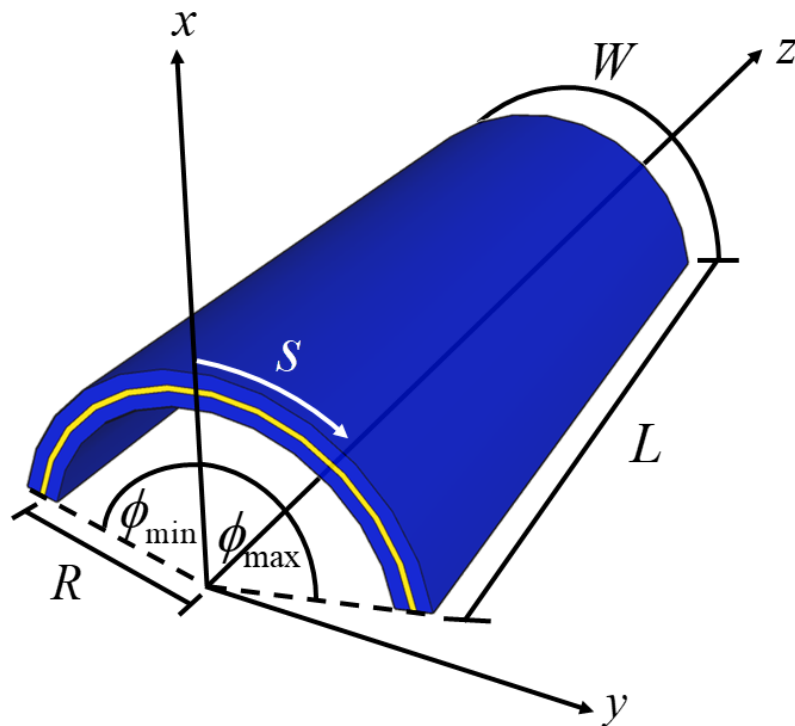
Figure 4. A schematic representation of a curved surface with a constant radius R [56]

$$\hat{H}_0 \Psi_0 = E_0 \Psi_0,$$
(3.1)

where $\hat{H}_0, E_0$ and Ψ_0 are Hamiltonian, the energy, and the wavefunction respectively. In the cylindrical coordinate, we can write the Hamiltonian of such a system as follows

$$\hat{H}_0 = -\frac{\hbar^2}{2\mu}\left(\frac{1}{R^2}\frac{\partial^2}{\partial\phi^2} + \frac{\partial^2}{\partial z^2}\right) - \frac{\upsilon_R\hbar^2}{8\mu R^2} + V_C(\phi,z), \tag{3.2}$$

which the derivation is in Appendix A. The initial term is the kinetic energy operator, where μ denotes an electron's effective mass. The second term is the geometric potential, where υ_R denotes a constant that accounts for the effects of strain and curvature in the system. These two terms are corresponding to the Hamiltonian of a particle bound on a curved surface. The system's confinement potential V_C is

$$V_C(\phi,z) = \begin{cases} 0, & \phi_{\min} \le \phi \le \phi_{\max} \cap 0 \le z \le L \\ \infty, & \text{otherwise} \end{cases}. \tag{3.3}$$

Therefore, the Hamiltonian in equation (3.2) is substituted into equation (3.1), we obtain

$$-\frac{\hbar^2}{2\mu}\left(\frac{1}{R^2}\frac{\partial^2}{\partial\phi^2} + \frac{\partial^2}{\partial z^2}\right)\Psi_0 - \frac{\upsilon_R\hbar^2}{8\mu R^2}\Psi_0 + V_C\Psi_0 = E_0\Psi_0. \tag{3.4}$$

Equation (3.4) is second order differential equation which can be solved analytically as shown in Appendix B. Finally, we acquire the system's energy level and normalized wavefunction as

$$E_0 = \frac{n_\phi^2\pi^2\hbar^2}{2\mu W^2} + \frac{n_z^2\pi^2\hbar^2}{2\mu L^2} - \frac{\upsilon_R\hbar^2}{8\mu R^2} \tag{3.5}$$

and

$$\Psi_0 = \frac{2}{\sqrt{WL}}\sin\left(\frac{n_\phi\pi R}{W}(\phi-\phi_{\min})\right)\sin\left(\frac{n_z\pi}{L}(z-z_{\min})\right), \tag{3.6}$$

where n_ϕ and n_z are a positive integer from 1 to infinity.

A curved surface electron system with a donor impurity and an external electric field

As demonstrated, the energy level and wavefunction of a system can be calculated analytically in the absence of a donor impurity and an external electric field. The Hamiltonian system becomes more complicated when disturbances are added to the system. Let us consider the Hamiltonian $\hat{H}_D$ of the following system as

$$\hat{H}_D = -\frac{\hbar^2}{2\mu}\left(\frac{1}{R^2}\frac{\partial^2}{\partial\phi^2} + \frac{\partial^2}{\partial z^2}\right) - \frac{\upsilon_R\hbar^2}{8\mu R^2} + V_C(\phi,z) + V_D(\phi,z) + V_F(\phi). \tag{3.7}$$

V_D and V_F, which are subtracted from the original Hamiltonian $\hat{H}_0$, are the potential due to a donor impurity and an electric field respectively. This type of doping generates

a coulomb force in the vicinity of the dopant. The Coulomb effect V_D between an electron and a donor position is represented by

$$V_D = \frac{-e^2}{4\pi\varepsilon_0\varepsilon r'},$$ (3.8)

where $-e$ indicates the electron charge. ε is relative permittivity of GaAs relating to the vacuum permittivity ε_0. r' is the range between a donor and a carrier particle, is expressed by $r' = \sqrt{R^2\left[2 - 2\cos(\phi - \phi_D)\right] + (z - z_D)^2}$. ϕ_D and z_D are the coordinates of a donor in the ϕ-axis and the z-axis, respectively. Consequently, the position of a donor in s coordinate is $s_D = R\phi_D$. The electric field $\vec{F}$ which perturbs the system is perpendicular to the plane of surface. $\vec{F}$ and the x-axis are at an angle ϕ_F where $\vec{F} = F\cos\phi_F\hat{i} + F\sin\phi_F\hat{j}$. V_F is obtained from the relation between V_F and $\vec{F}$ $\left(e\vec{F} = -\vec{\nabla}V_F\right)$, given by

$$V_F(\phi) = eFR\cos(\phi - \phi_F).$$ (3.9)

Due to the addition of parameters, the Schrödinger equation with this Hamiltonian cannot be easily solved analytically. As a result, this problem is solved numerically using the finite difference approach. We convert these parameters to dimensionless quantities by measuring the length and the energy in the unit of the effective Bohr radius $a^* = \frac{4\pi\varepsilon_0\varepsilon\hbar^2}{\mu e^2}$ and the effective Rydberg energy $R^* = \frac{\mu e^4}{8(\varepsilon_0\varepsilon h)^2}$; therefore, The dimensionless Schrödinger equation is $\tilde{H}_D\Psi_D = \tilde{E}_D\Psi_D$ where

$$\tilde{H}_D = -\left(\frac{1}{\tilde{R}^2}\frac{\partial^2}{\partial\phi^2} + \frac{\partial^2}{\partial\tilde{z}^2}\right) - \frac{\upsilon_R}{4\tilde{R}^2} + \tilde{V}_C(\phi,\tilde{z}) + \tilde{V}_D(\phi,\tilde{z}) + \tilde{V}_F(\phi).$$ (3.10)

Ψ_D and $\tilde{E}_D = \frac{E_D}{R^*}$ are wavefunctions and energy levels of the following system respectively. The length parameters R and z in equation (3.7) become $\tilde{R} = \frac{R}{a^*}$ and $\tilde{z} = \frac{z}{a^*}$. Three potentials $\tilde{V}_C$, $\tilde{V}_D$ and $\tilde{V}_F$ in equation (3.10) are measured in the same unit which $\tilde{V}_C = \frac{V_C}{R^*}$,

$$\tilde{V}_D = \frac{V_D}{R^*} = \frac{-2}{\sqrt{\tilde{R}^2\left[2 - 2\cos(\phi - \phi_D) + (\tilde{z} - \tilde{z}_D)^2\right]}},$$ (3.11)

and

$$\tilde{V}_F = \frac{V_F}{R^*} = \tilde{F}\tilde{R}\cos\left(\phi - \phi_F\right),$$

(3.12)

where the dimensionless strength of an electric field is $\tilde{F} = \dfrac{F}{F^*}$ and $F^* = \dfrac{\hbar^2}{2e\mu\left(a^*\right)^3}$.

Following that, the variables have been already converted to dimensionless form. We use the dimensionless Schrödinger equation to compute the energy levels $\tilde{E}_D$ and wavefunctions Ψ_D by finite difference method. Finally, the binding energy $\tilde{E}_B$ is calculated from the difference between the energy without and with a donor impurity,

$$\tilde{E}_B = \tilde{E}_0 - \tilde{E}_D.$$

(3.13)

The dimensionless form of E_0 in equation (3.5) is

$$\tilde{E}_0 = \frac{n_\phi^2\pi^2}{\left(W/a^*\right)^2} + \frac{n_z^2\pi^2}{\left(L/a^*\right)^2} - \frac{\upsilon_R}{4\left(R/a^*\right)^2},$$

(3.14)

Finite difference method for a two-dimensional curved surface

The finite difference method is a numerical approach used to solve differential equations. It may be used to solve the Schrödinger equation in a variety of two-dimensional electron systems. Therefore, such method is chosen to solve the problem of curved surface with a donor impurity as well. In the beginning, we create the uniform grid on the $s-z$ plane, which has the $N_\phi \times N_z$ intersections, and s denotes the coordinates along the arc of circle. Following that, we use the central difference approximation to derive the derivative between the grid points. The Schrödinger equation $\tilde{H}_D\Psi_D = \tilde{E}_D\Psi_D$ becomes

$$-\frac{1}{\tilde{R}^2(\Delta\phi)^2}\left(\Psi_D^{i-1,j} - 2\Psi_D^{i,j} + \Psi_D^{i+1,j}\right)$$
$$-\frac{1}{(\Delta\tilde{z})^2}\left(\Psi_D^{i,j-1} - 2\Psi_D^{i,j} + \Psi_D^{i,j+1}\right)$$
$$+\left(\tilde{V}_C^{i,j} + \tilde{V}_D^{i,j} + \tilde{V}_F^{i,j} - \frac{\upsilon_R}{4\tilde{R}^2}\right)\Psi_D^{i,j} = \tilde{E}_D\Psi_D^{i,j}$$

(3.15)

where i and j are indices specifying the positions of the grid intersections along ϕ, z-axis. $\Psi_D^{i,j}$ denotes the wavefunction at the position i, j. $\tilde{V}_C^{i,j}$, $\tilde{V}_D^{i,j}$, and $\tilde{V}_F^{i,j}$ are dimensionless potentials at the point i, j as well. Since this divided grid contains $N_\phi \times N_z$ points, we can formulate $\left(N_\phi \times N_z\right)^2$ differential equations. This can be represented as the following equation matrix:

$$
\begin{bmatrix}
\delta_{11}-\tilde{E}_D & v_{12} & 0 & \cdots & \cdots & \cdots & \cdots & \cdots & \cdots & \cdots & \cdots & \cdots & 0 & 0 & 0 \\
v_{11} & \delta_{12}-\tilde{E}_D & v_{13} & 0 & \cdots & \cdots & \cdots & \cdots & \cdots & \cdots & \cdots & \cdots & 0 & 0 & 0 \\
0 & v_{12} & \delta_{13}-\tilde{E}_D & v_{14} & 0 & \cdots & \cdots & \cdots & \cdots & \cdots & \cdots & \cdots & 0 & 0 & 0 \\
\vdots & \vdots & v_{13} & \mu_{21} & \mu_{22} & \mu_{23} & \vdots & \vdots & \vdots & \vdots & \vdots & \vdots & \vdots & \vdots & \vdots \\
\mu_{21} & \mu_{22} & \mu_{23} & \vdots & \vdots & \vdots & \vdots & \vdots & \vdots & \vdots & \vdots & \vdots & \vdots & \vdots & \vdots \\
\vdots & \vdots & \vdots & \vdots & \vdots & \vdots & \vdots & \vdots & \vdots & \mu_{N_\phi-1,N_z-2} & \mu_{N_\phi-1,N_z-1} & \mu_{N_\phi-1,N_z} & \vdots & \vdots & \vdots \\
\vdots & \vdots & \vdots & \vdots & \vdots & \vdots & \vdots & \vdots & \vdots & \vdots & \vdots & 0 & v_{N_\phi,N_z-3} & 0 & \vdots \\
0 & 0 & 0 & \vdots & \vdots & \vdots & \vdots & \vdots & \vdots & \vdots & \mu_{N_\phi,N_z-2} & 0 & \delta_{N_\phi,N_z-2}-\tilde{E}_D & v_{N_\phi,N_z-1} & v_{N_\phi,N_z-2} \\
0 & 0 & 0 & \vdots & \vdots & \vdots & \vdots & \vdots & \vdots & \vdots & \mu_{N_\phi,N_z-1} & 0 & v_{N_\phi,N_z-2} & \delta_{N_\phi,N_z-1}-\tilde{E}_D & v_{N_\phi,N_z-1} \\
0 & 0 & 0 & \vdots & \vdots & \vdots & \vdots & \vdots & \vdots & \vdots & \mu_{N_\phi,N_z} & 0 & v_{N_\phi,N_z} & v_{N_\phi,N_z-1} & \delta_{N_\phi,N_z}-\tilde{E}_D
\end{bmatrix}
\begin{bmatrix}
\Psi_D^{11} \\
\Psi_D^{12} \\
\Psi_D^{13} \\
\Psi_D^{14} \\
\vdots \\
\vdots \\
\Psi_D^{N_\phi,N_z-3} \\
\Psi_D^{N_\phi,N_z-2} \\
\Psi_D^{N_\phi,N_z-1} \\
\Psi_D^{N_\phi,N_z}
\end{bmatrix}
= 0
$$

(3.16)

by defining $\delta_{ij} \equiv 0$, $u_{ij} \equiv 1$, and $v_{ij} \equiv 2$. Eventually, we acquire dimensionless energy levels $\tilde{E}_D$ and wavefunctions $\Psi_D^{i,j}$ by solving equation (3.16).

Our numerical results for the system without a donor and an electric field approach the solution in equation (3.14). This result demonstrates the validity of our numerical technique. The next chapter will provide another method for verifying our numerical results.

Oscillator strength in a curved surface system

In a curved surface system, The Thomas-Reiche-Kuhn (TRK) sum rule is also useful for the system. For derivation, we begin with two commutation relations,

$$\left[\hat{e}_\phi p_\phi , \hat{e}_\phi R \right] = \frac{\hbar}{i} \tag{3.17}$$

and

$$\left[H , \hat{e}_\rho R \right] = \frac{\hbar}{\mu i}\left(\hat{e}_\phi p_\phi + \hat{e}_\rho \frac{i\hbar}{2R} \right). \tag{3.18}$$

μ and $\hbar$ are an electron's effective mass and the reduced Planck constant, respectively. R is the radius of the curved surface. $\hat{e}_\rho$ and $\hat{e}_\phi$ are the unit vectors of the cylindrical coordinate along the ρ- and ϕ- axis, respectively. The operator p_ϕ is the momentum along the ϕ-axis. In two-dimensional curved surface, the Hamiltonian can be written as $H = -\frac{\hbar^2}{2\mu}\left(\frac{1}{R^2}\frac{\partial^2}{\partial\phi^2} + \frac{\partial^2}{\partial z^2} \right) - \frac{\hbar^2}{8\mu R^2}$. If a commutator $\left[\hat{e}_\phi \hat{p}_\phi , \hat{e}_\rho R \right]$ in equation (3.17) is calculated and inserted a complete set of states, we will obtain

$$\langle n | \hat{e}_\phi p_\phi \cdot \hat{e}_\rho R - \hat{e}_\rho R \cdot \hat{e}_\phi p_\phi | n \rangle = \sum_m \left(\langle n | \hat{e}_\phi p_\phi | m \rangle \cdot \langle m | \hat{e}_\rho R | n \rangle - \langle n | \hat{e}_\rho R | m \rangle \cdot \langle m | \hat{e}_\phi p_\phi | n \rangle \right)$$

(3.19)

$|n\rangle$ and $|m\rangle$ are two arbitrary quantum states which are orthogonal. After the calculation, the relation in equation (3.18) can be written as

$$\langle n | \hat{e}_\phi p_\phi | m \rangle = \frac{\mu i}{\hbar}\left(E_n - E_m \right)\langle n | \hat{e}_\rho R | m \rangle - \langle n | \hat{e}_\rho \frac{i\hbar}{2R} | m \rangle \tag{3.20}$$

and

$$\langle m | \hat{e}_\phi p_\phi | n \rangle = \frac{\mu i}{\hbar}\left(E_m - E_n \right)\langle m | \hat{e}_\rho R | n \rangle - \langle m | \hat{e}_\rho \frac{i\hbar}{2R} | n \rangle. \tag{3.21}$$

E_n and E_m are the eigenstates of states $|n\rangle$ and $|m\rangle$, respectively. By substituting equation (3.20) and (3.21) into equation (3.19), the desired result is

$$\frac{\hbar^2}{2\mu} = \sum_m \left(E_m - E_n\right)\left|\langle m|\hat{e}_\rho R|n\rangle\right|^2.$$

(3.22)

Equation (3.22) leads to the important condition of the oscillator strength in a two-dimensional curved surface system,

$$1 = \frac{2\mu}{\hbar^2} \sum_m \left(E_m - E_n\right)\left|\langle m|\hat{e}_\rho R|n\rangle\right|^2,$$

(3.23)

or

$$1 = \frac{2\mu}{\hbar^2} \sum_m \left(E_m - E_n\right)\left|\langle m|\hat{e}_x R\cos\phi + \hat{e}_y R\cos\phi|n\rangle\right|^2.$$

(3.24)

$\hat{e}_\rho R$ is equal to $\hat{e}_x R\cos\phi + \hat{e}_y R\sin\phi$ in a Cartesian coordinate system. $\hat{e}_x$ and $\hat{e}_y$ are the unit vectors of the coordinate. Since this dissertation focuses on the incident light polarized along the x- and y-direction (ϕ-axis), equation (3.24) confirms that the summation of the oscillator strength from state $|n\rangle$ to all states $|m\rangle$ along both directions is exactly one. By comparing equation (3.24) with equations (2.33) and (2.34), it is found that the sum rule of the curved surface system is different from that of the flat surface system.

CHAPTER 4 RESULTS AND DISCUSSION

Effects of a donor impurity on a curved surface at various locations

In this computation, the physical parameters are $\mu = 0.067 m_0$, L = 300 nm, υ_R = 6 [31] and ε = 12.4, correlating with a^* = 9.79 nm, R^* = 5.929 meV, and F^* = 6.054 $\times$ 10^5 V/m. This work focuses on the binding energy values with different donor locations by adjusting the radius R, width W and electric field F. A top view of the curved surface and marks of impurity location are displayed in Figure 5. Both sides of the surface are positioned at $s = -0.5W$ and $s = 0.5W$, respectively. We investigate eight impurity locations consisting of $(s_D, z_D) = (0, 0.5L)$, $(0.25W, 0.5L)$, $(0.5W, 0.5L)$, $(0.5W, 0.75L)$, $(0.5W, L)$, $(0.25W, L)$, $(0, L)$, and $(0, 0.75L)$, marked by 1-8 numbers.
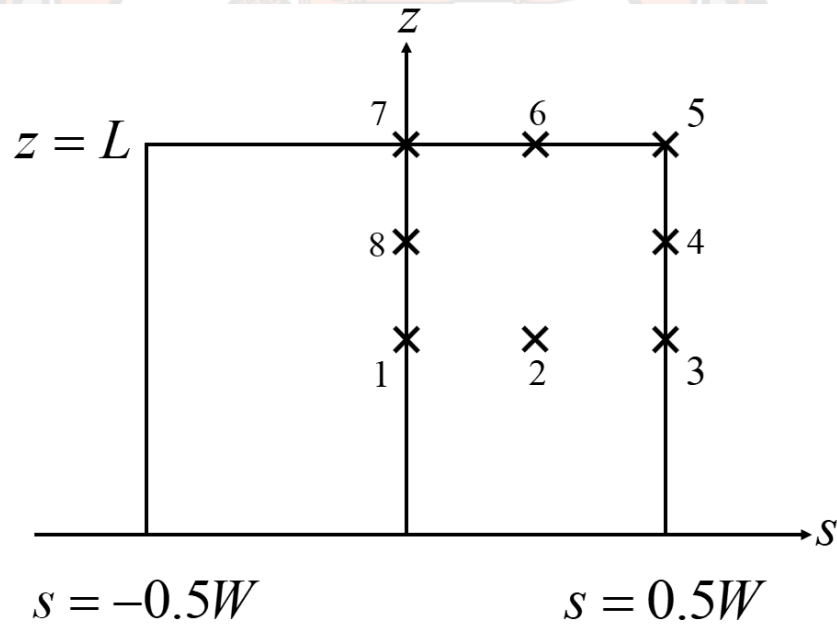
Figure 5. On the s-z plane, a curved surface with length L and width W. Numbers 1–8 are assigned to eight impurity locations denoted by cross signs. [56]

The effect of curvature on the system's energy levels E_D in Figure 6 shows that the energy levels of both the ground state and the first excited state converge to specific values in the case of an increasing surface radius. With W = 150 nm, the system's

energy levels converge to the exact dimensionless energy of a two-dimensional hydrogen atom [45, 46] equal to

$$E_D = -\frac{R^*}{\left(n-\frac{1}{2}\right)^2},$$ (4.1)

where n is a positive integer. Figure 6 illustrates that the energies of the ground and first excited states are close to $-4R^*$ and $-4R^*/9$, respectively. This result also confirms the computational results discussed in the previous chapter. However, while the surface radius decreases until reaching the Bohr radius a^*, the energy levels drop rapidly. They go to a minimum when the surface nearly completes the full circle at $R = W/2\pi$. Since the negative potentials (Coulomb and geometric potentials) dominate when the surface radius R is small.
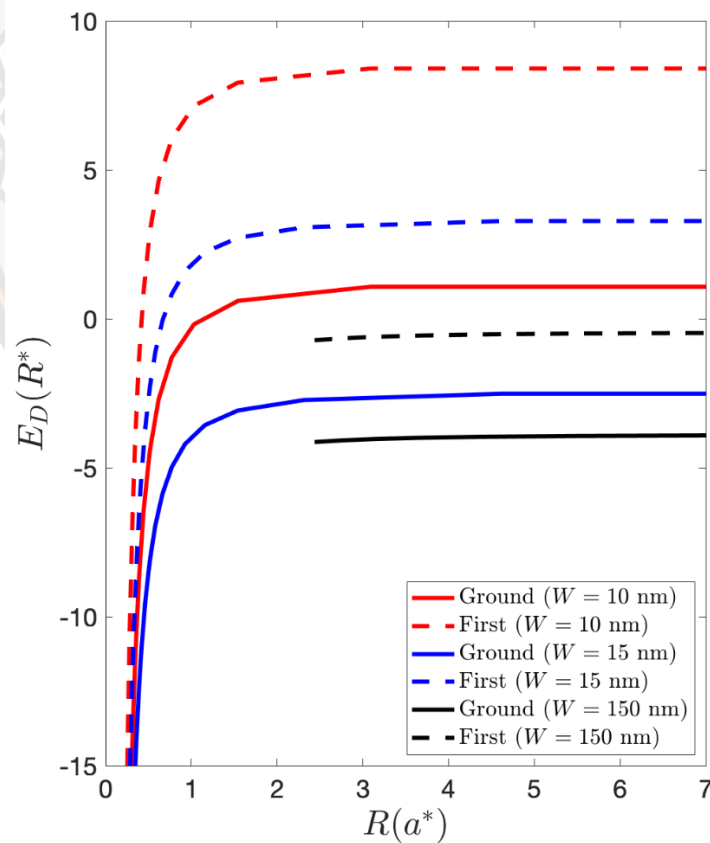
Figure 6. The energies E_D of the ground and first excited states of a curved surface with an on-center donor $\left(\phi_D = 0, z_D = 0.5L\right)$ impurity are plotted as a function of the radius R for widths W of 10, 15, and 150 nm. [56]

Figure 7 displays the binding energies in eight donor locations, with each sub-graph comprising red (W = 10 nm), blue (W = 50 nm), and black (W = 150 nm) lines. Overall, the binding energies are more heightened when the width of the curved surface is narrow (W = 10 nm). Those binding energies are relatively high in locations 1, 2, and 8 because a donor has a more critical effect on E_D than in other locations. In contrast, the binding energies at locations 5, 6, and 7 are weak in all sample widths W since the confinement at the top region reduces the impact of Coulomb potential from a donor. Additionally, the change of width W slightly affects such binding energies. The binding energies of the ground state and the first excited state at each location are similar compared to the case of R = 30 nm (Figure 7(a) and (b)) and R = 23.87 nm (Figure 7(c) and (d)). Nonetheless, there is a noticeable difference in first excited state binding energies in Figure 7(d) when a donor is positioned on locations 3 and 4. The binding energies of W = 150 nm are more significant than those of W = 50 nm at those locations.
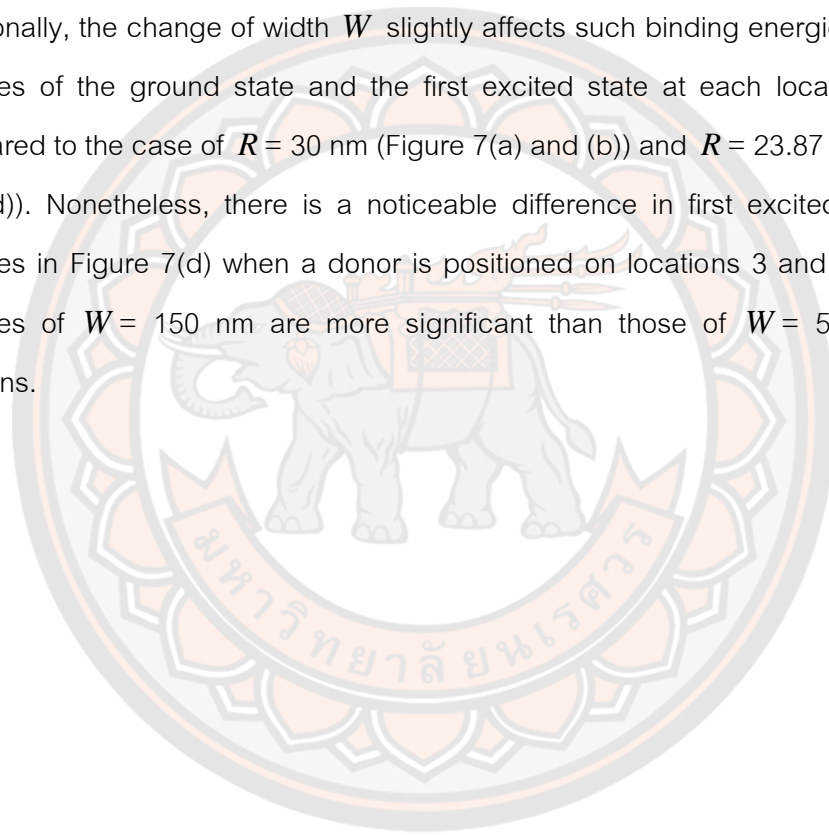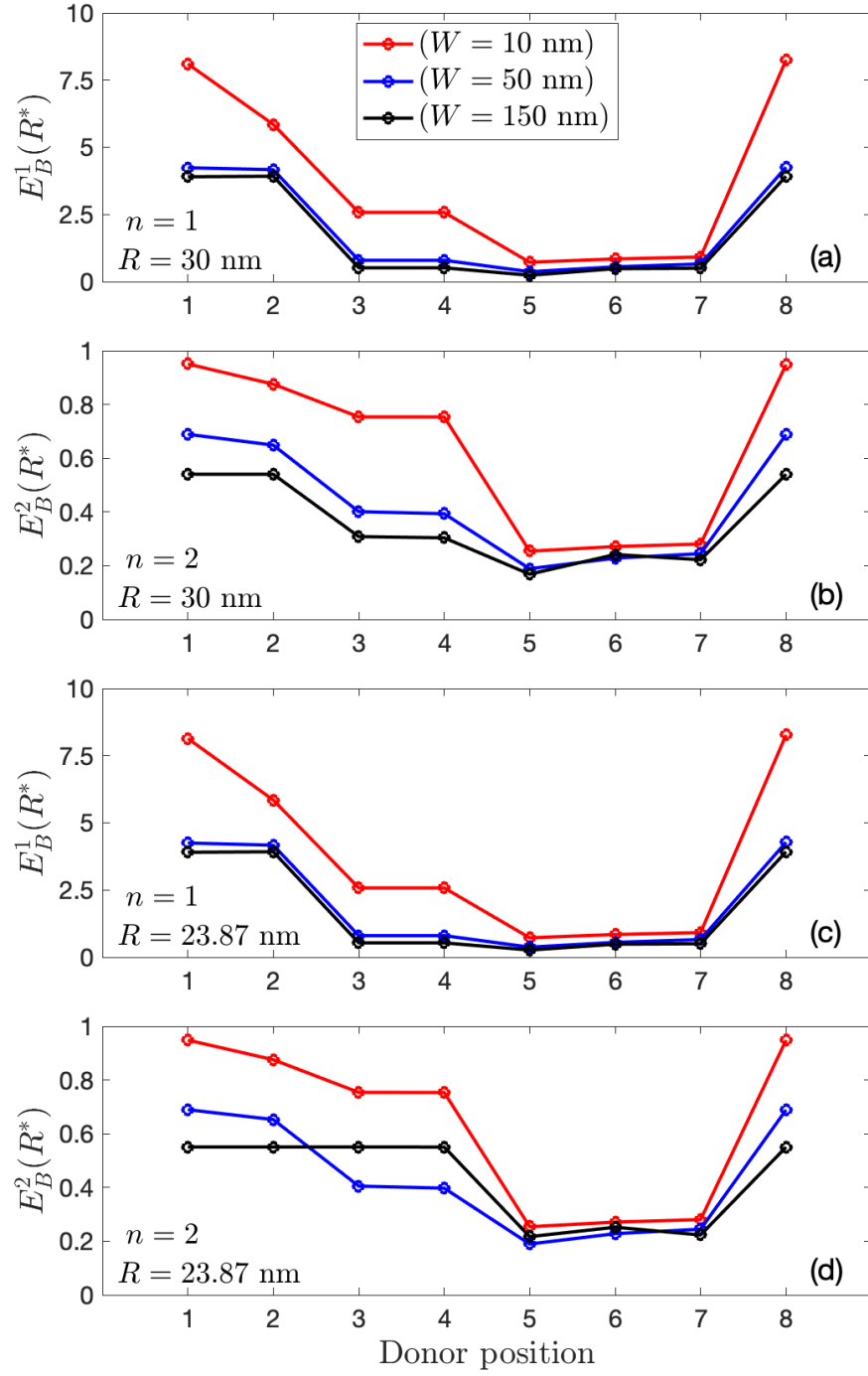
Figure 7. Binding energies E_B^n of the ground $(n=1)$ and first excited states $(n=2)$ in a curved surface with R = 30 nm ((a) and (b)) and R = 23.87 nm ((c) and (d)), respectively. The numbers on the x-axis correspond to the eight donor locations illustrated in Figure 5. [56]

The impressive result in Figure 7(d) leads the researcher to further study a curved surface with a donor in location 3 by comparing the binding energies of each width at various radius values. Figure 8 shows that in the case of widths W = 10, 20, and 50 nm, the binding energies of both the ground state (a) and the first excited state (b) are stable at the specific values when the curvature radius R is large. Nevertheless, those binding energies peak if the curved surface is almost circular since two negative potentials (geometric and Coulomb potentials) are outstanding when R is sufficiently small. On the other hand, the results of widths W = 150 and 200 nm are slightly different, and the ground state binding energies are unvarying for all reasonable radius values. Conversely, the first excited state binding energies surprisingly rocket higher than that of W = 50 nm.
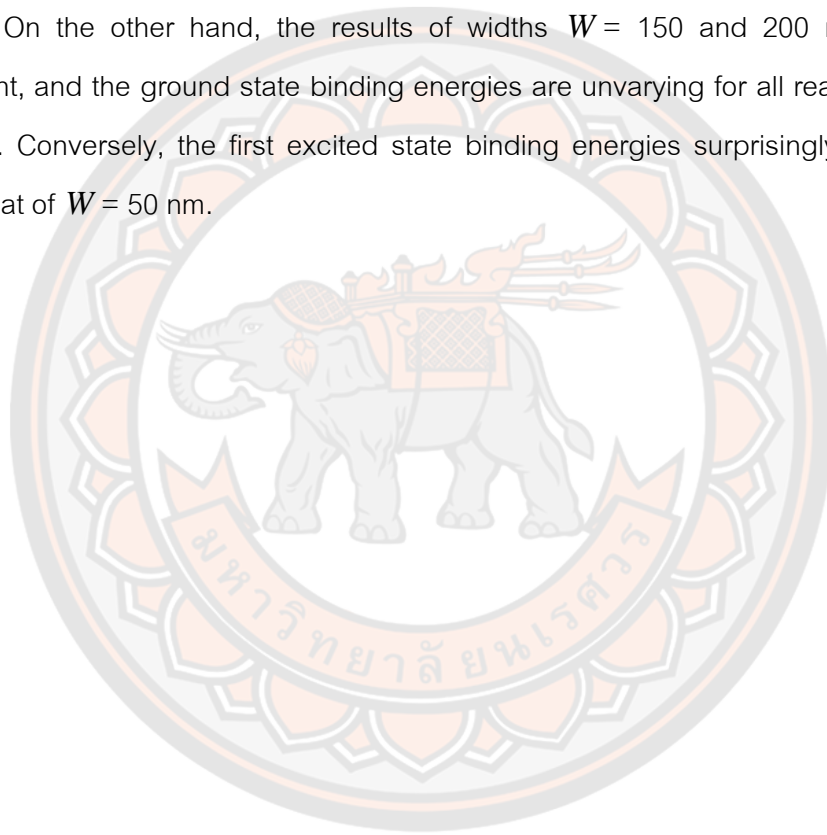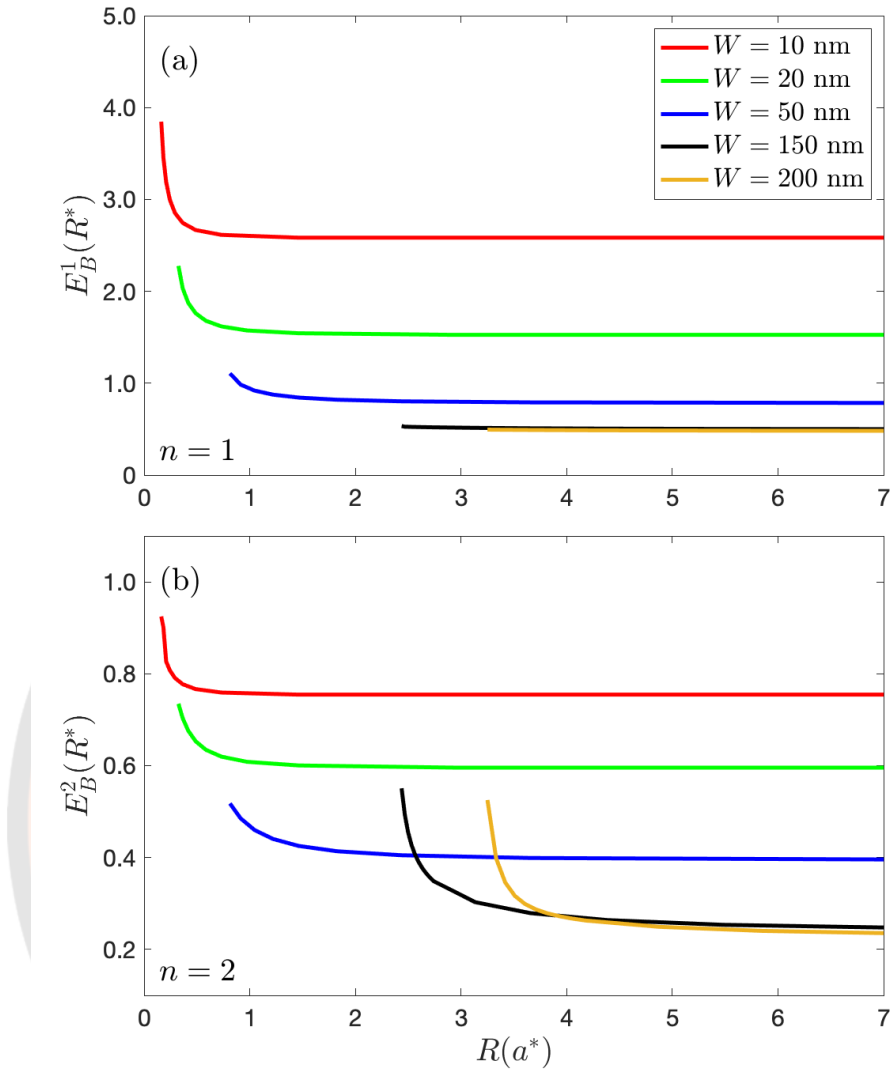
Figure 8. Binding energies E_B^n of the ground $(n=1)$ and first excited states $(n=2)$ in a curved surface with a donor impurity in location 3 as a function of the radius R for widths W (10, 20, 50, 150, and 200 nm). [56]

Electron distributions can clarify unusual characteristics of those binding energies. Figure 9 shows the probability densities on the s-z plane relating to the binding energies in Figure 8. Figure 9(a-f) illustrates that the electron distributions of the ground state and first excited state with tiny width W slightly shift to the left side when the radius R decreases. Those distributions in Figure 9(a) and (d) nearly become symmetric because a donor at location 3 produces almost equivalent Coulomb potential wells, which enhance the confinement on each side of a surface. Consequently, the

binding energies of the first two states with narrow widths W tend to be high when a curved surface approaches a full circle. However, peaks of the binding energies with a wide surface (W = 150 and 200 nm) arise differently. In Figure 9(i), the electron distribution has a peak oriented vertically (z-axis) at the top and bottom, localized around a donor at location 3. The distribution form gradually changes as the radius R decreases, as seen in Figure 9(g) and (h). Finally, that distribution completely transforms to arrange along the s-axis, in which electron probability distributes both left and right sides equally. Not only the remarkable effect of the Coulomb potential V_D with small R affects the first excited state binding energies, but also the transformation of distribution has a massive effect on those binding energies since the average distance from an electron to a donor in Figure 9(g) is shorter than in Figure 9(i).
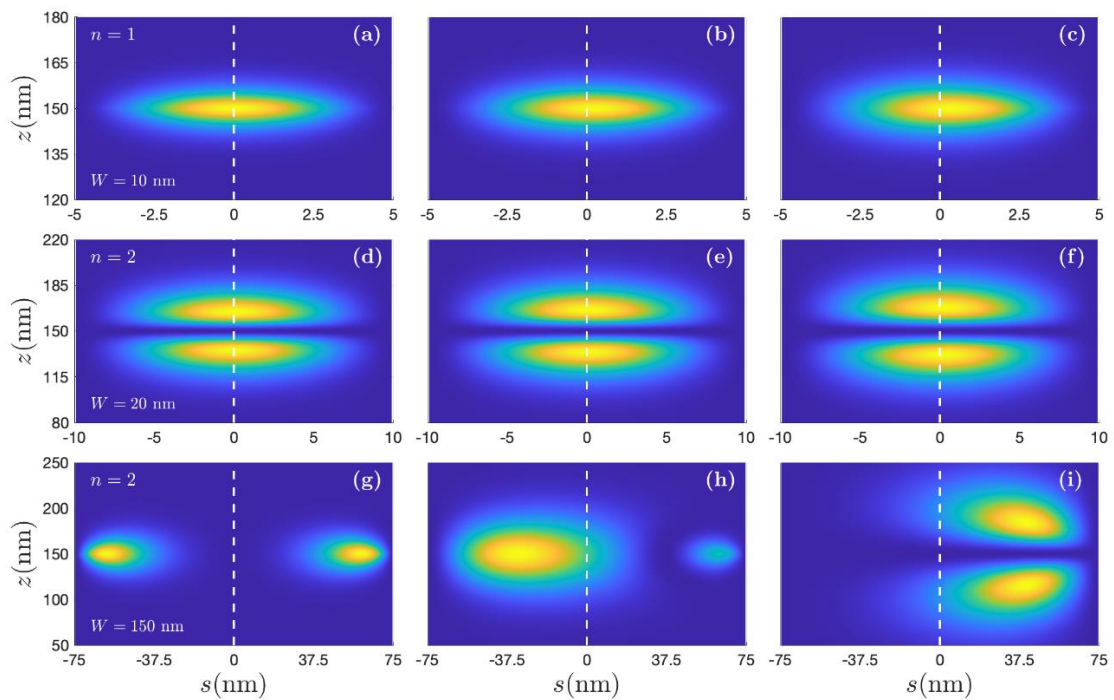
Figure 9. (a-c) Electron distributions of the ground states Ψ_D^1 for a curved surface with W = 10 nm and R = 1.6, 2.8, and 14.6 nm, respectively. (d-f) Electron distributions of the first excited states Ψ_D^2 for a curved surface with W = 20 nm and R = 3.3, 4.2, and 14.6 nm, respectively. (g-i) Electron distributions of the first excited states Ψ_D^2 for a curved surface with W = 150 nm and R = 24.4, 31.2, and 109.7 nm, respectively. Note

that R values in (a), (d), and (g) are the lowest for each system, and a donor is at location 3 in all figures. [56]

Effects of an electric field on donor states

This section will explore the impacts of an electric field on the binding energies. In Figure 10 to Figure 13, we are interested in a curved surface with R = 23.87 nm for W = 35, 75, and 115 nm relating to ϕ_m = 0.73, 1.57, and 2.41 rad. A given electric field is along the x- and y-axis, matching ϕ_F = 0, 0.5π, π, and 1.5π rad.

The results in Figure 10 demonstrate that an electric field in the ±x-direction and various widths W have unpredictable effects on the binding energies at each donor location. In Figure 11, electron distributions of ground and first excited states without a donor impurity for widths W = 35 and 115 nm can describe those results. The confinement due to such a donor are high when a donor is positioned near a peak of probability distribution. As a result, the binding energies are incredible in those situations. For instance, the binding energies at donor locations 1, 2 and 8 for W = 35 nm relatively high in Figure 10(a) and (b) because an electron probability is significantly high around those regions, as shown in Figure 11(a) and (b). Conversely, the binding energies at donor locations 3 and 4 for W = 115 nm are dominant instead of locations 1, 2, and 8 in Figure 10(a) and (b) since an electric field in the positive x-direction separates electron distributions into both left and right sides of a surface. Therefore, donor locations 3 and 4 are nearer points from the peak of electron probability, as displayed in Figure 11(c) and (d).
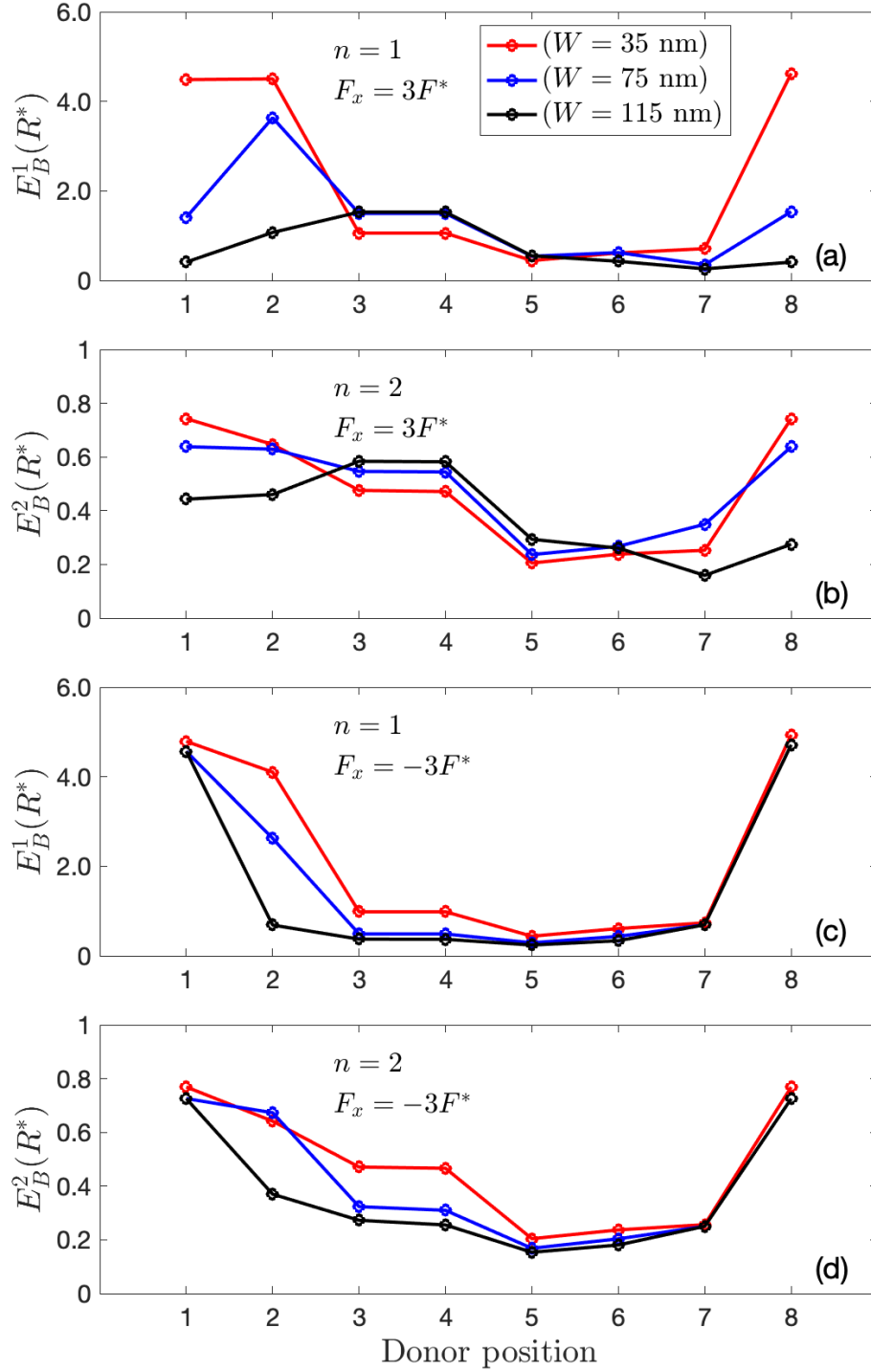
Figure 10. Binding energies E_B^n of the ground state (a) and first excited state (b) for W = 35, 75, and 115 nm with an electric field $\vec{F} = 3F^*\hat{i}$, and the ground state (c) and first excited state (d) binding energies for the same values of W with an electric field $\vec{F} = -3F^*\hat{i}$. The x-axis numbers correspond to eight donor locations. [56]
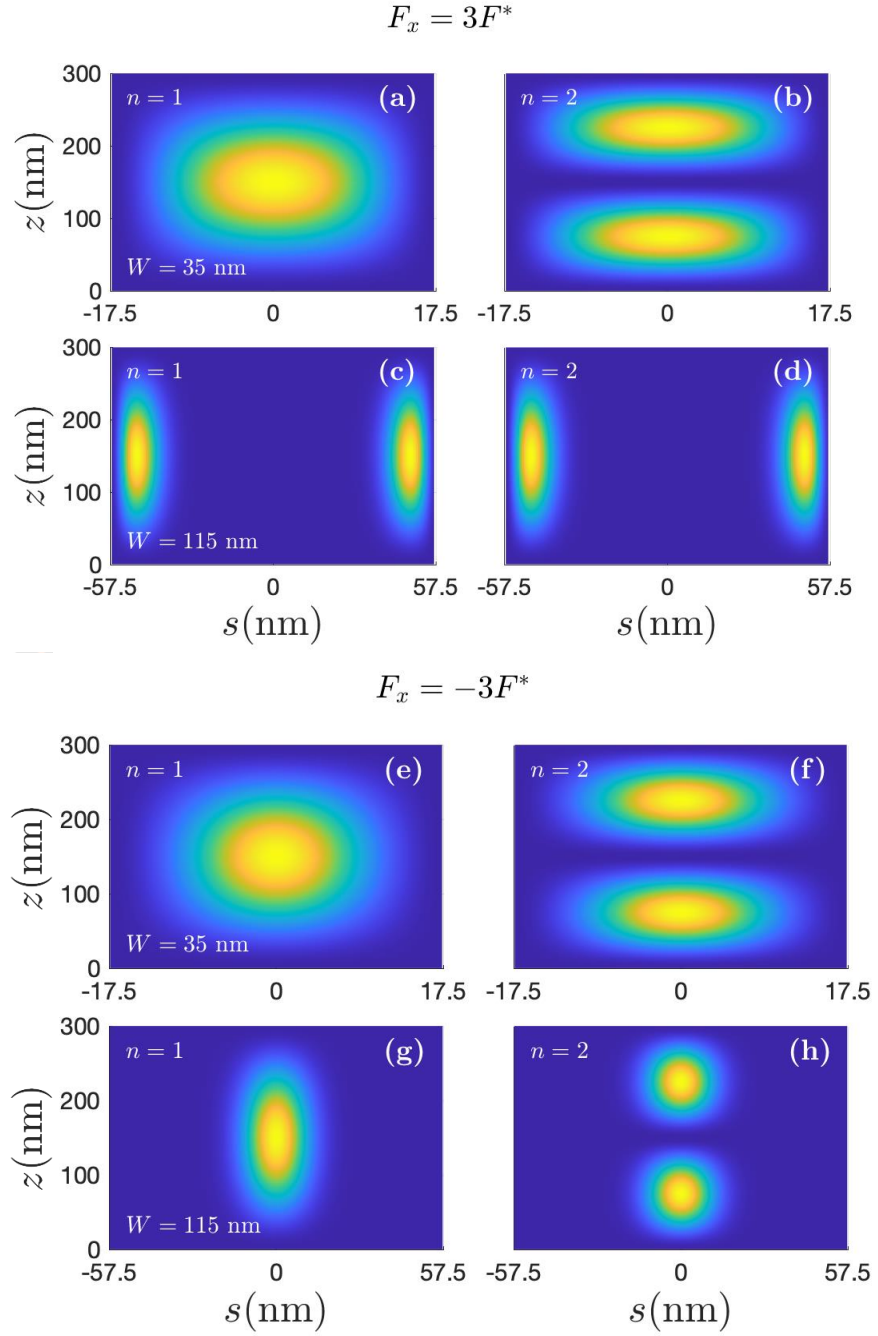
$$F_x = 3F^*$$

$$F_x = -3F^*$$

Figure 11. Electron distributions of the ground state (a) and first excited state (b) at $W = $ 35 nm as well as the ground state (c) and first excited state (d) at $W = $ 115 nm in the presence of an electric field $\vec{F} = 3F^*\hat{i}$. (e), (f), (g), and (h) illustrate those probability distributions with an electric field $\vec{F} = -3F^*\hat{i}$. [56]

Figure 11(e-f) shows that if an electric field turns to negative x-direction, the electron distributions move to the central line at $s = 0$ for $W = 35$ and 115 nm. Hence, the electric field supports the attractive force from a donor impurity on locations 1 and 8, but it reduces the capability to confine an electron when a donor is doped at locations 3 and 4. As a result of such distribution, the binding energies at donor locations 1 and 8 are similarly high in all three widths $W = 35$, 75, and 115 nm. Furthermore, the binding energies at locations 3 and 4 are relatively lower than the results in Figure 10(a) and (b).
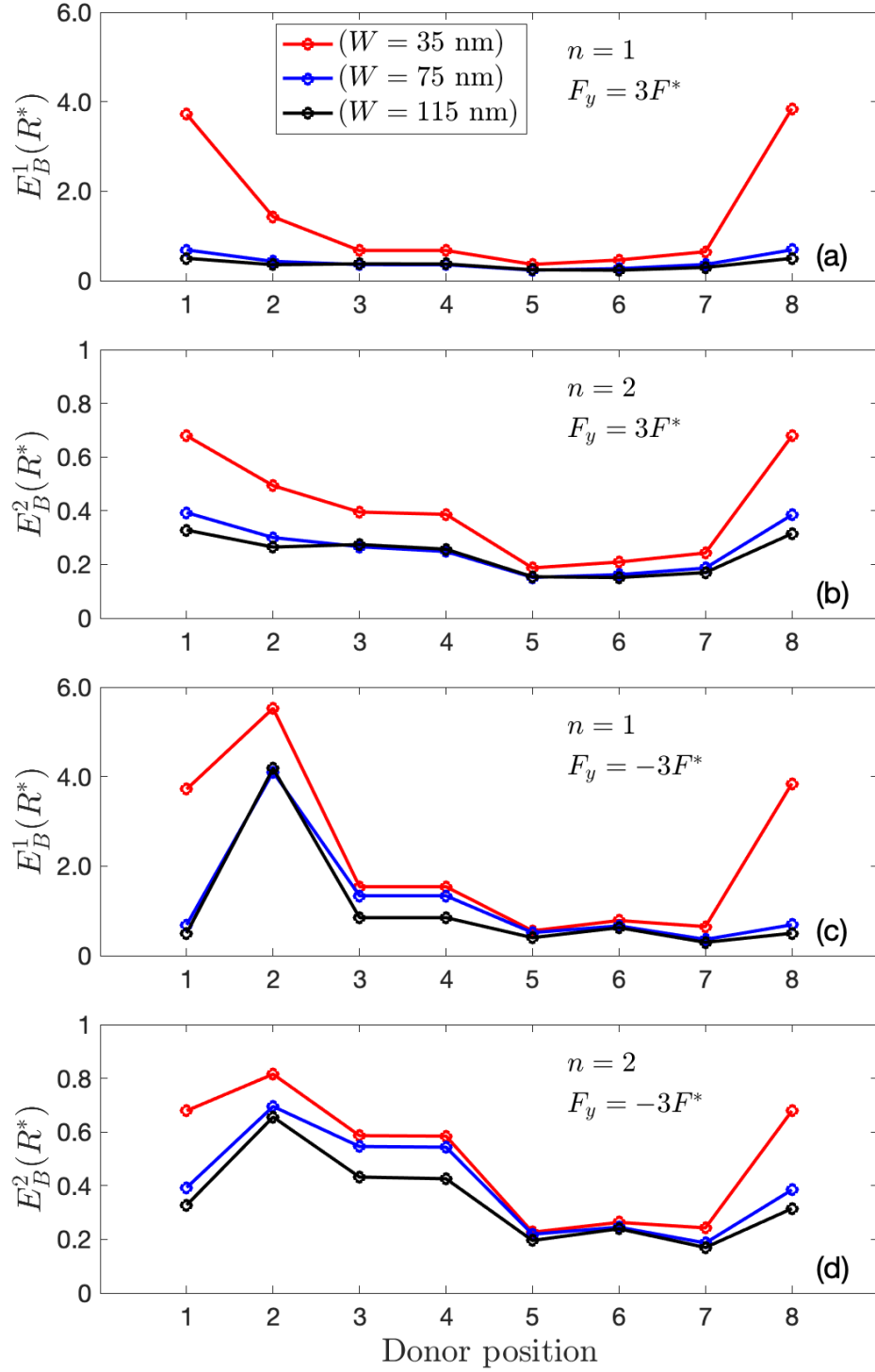
Figure 12. Binding energies E_B^n of the ground state (a) and first excited state (b) for W = 35, 75, and 115 nm with an electric field $\vec{F} = 3F^*\hat{j}$, and the ground state (c) and first excited state (d) binding energies for the same values of W with an electric field $\vec{F} = -3F^*\hat{j}$. The x-axis numbers correspond to eight donor locations. [56]

$$F_y = 3F^*$$

$$F_y = -3F^*$$
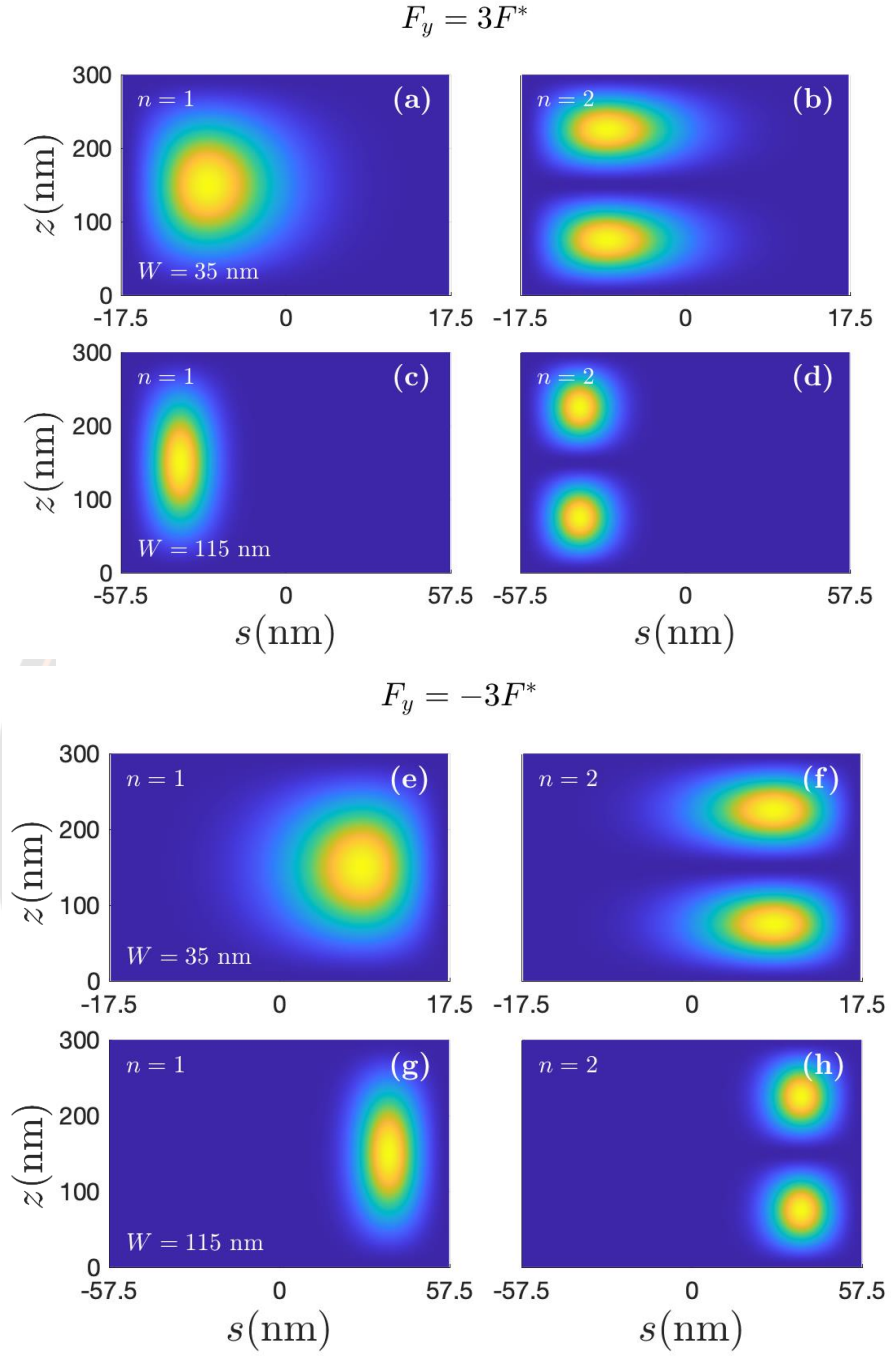
Figure 13. Electron distributions of the ground state (a) and first excited state (b) at $W = 35$ nm as well as the ground state (c) and first excited state (d) at $W = 115$ nm in the presence of an electric field $\vec{F} = 3F^*\hat{j}$. (e), (f), (g), and (h) illustrate those probability distributions with an electric field $\vec{F} = -3F^*\hat{j}$. [56]

Figure 12 illustrates the effect of an electric field in the y-direction on the binding energies. When the electric field is directed along the y-axis, the binding energies of W = 75 and 115 nm are relatively low at all locations since the field drives the electron distributions to the left side of a surface, as illustrated in Figure 11(c) and (d). Nevertheless, the binding energies of W = 35 nm at donor locations 1 and 8 are stronger than those at other locations because the tight confinement from V_C causes the average distance between a donor and an electron to slightly locomote from the original. In contrast, a negative y-direction electric field causes the electron distributions to shift to the right, as displayed in Figure 13(e–h). It results in the highest binding energies at location 2 for all widths W. Additionally, higher binding energies occur at locations 3 and 4. A shift of electron distributions to both left and right sides due to an electric field does not influence differently on the binding energies at locations 1, 7, and 8 because of the system's symmetry. Since an electric field in both the x- and y-directions cannot affects donor states at locations 5, 6, and 7, the binding energies at such locations in Figure 10 and Figure 12 are always low and little responsive to the width W.

Oscillator strength in a two-dimensional curved surface

This section will show the effects of curvature and an electric field on the oscillator strength of a curved surface. We study the oscillator strength of the electron transition between the ground state and the first excited state. An electric field at an angle ϕ_F is as displayed in Figure 14.
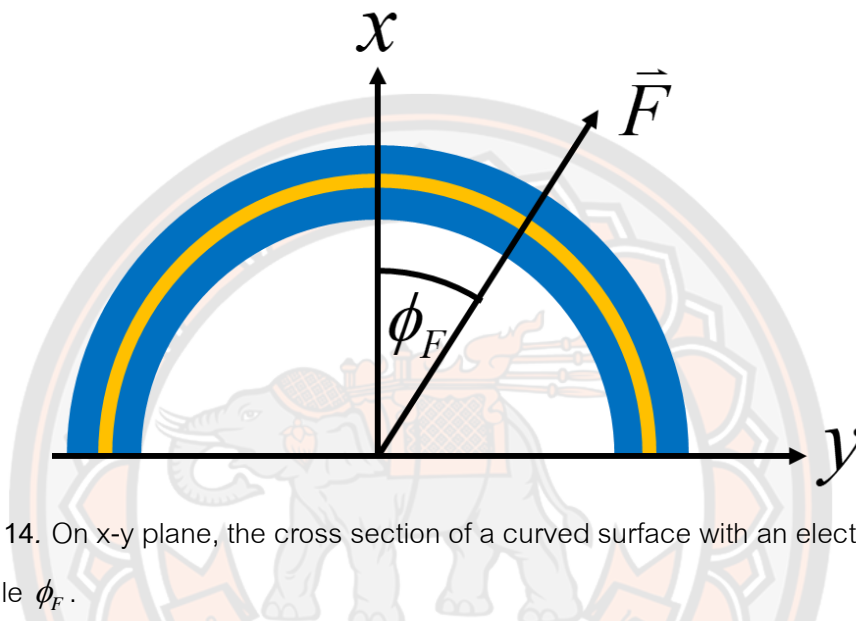
Figure 14. On x-y plane, the cross section of a curved surface with an electric field $\vec{F}$ at an angle ϕ_F.
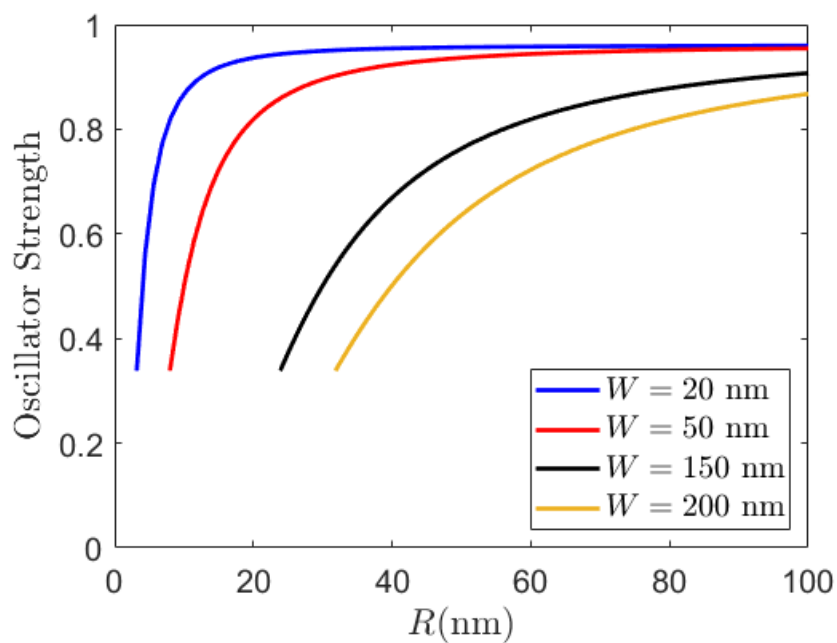
Figure 15. The oscillator strength along the y-direction of the ground and first excited states as a function of R with $W = 20, 50, 150$ and 200 nm, respectively.

Figure 15 shows the effect of a radius on the oscillator strength between the ground and first excited states with various widths W. We only report when the incident light is polarized in the y-direction because the curved surface is not sensitive to the x-polarized light for all radius values. Overall, decreasing R reduces the oscillator strength values of whole widths, but there is a difference between the tiny (W = 20 and 50 nm) and large (W = 150 and 200 nm) widths. The oscillator strength of wide W gradually declines while R decreases. For the narrow W, the curvature slightly influences the oscillator strength when R is significant, and then the oscillator strength drastically decreases when R reaches specific values. The oscillator strength declines because adding curvature causes the coupling between the ground and first excited states drops.
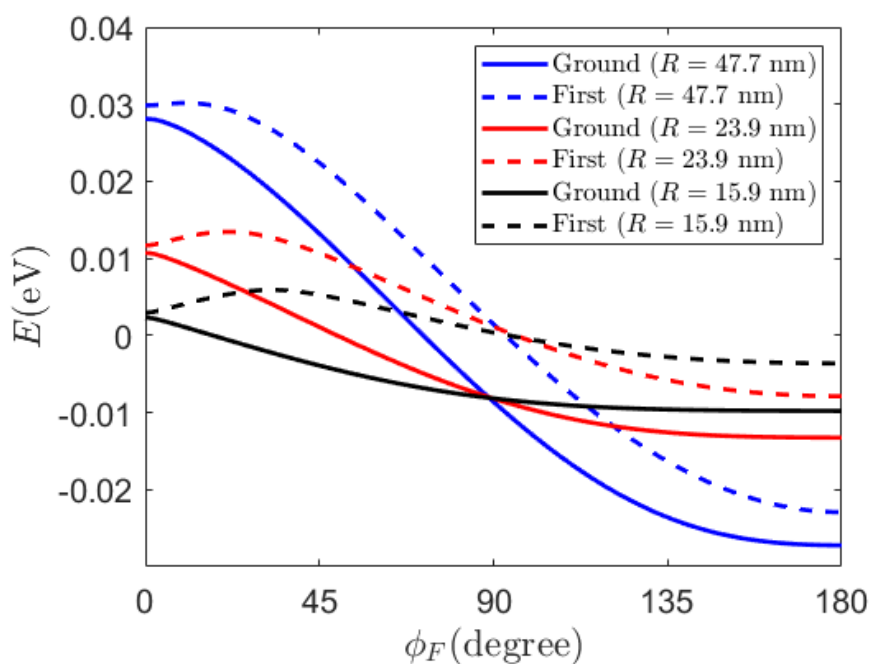
Figure 16. The energy levels of the ground and first excited states as a function of ϕ_F with R = 15.9, 23.9 and 47.7 nm, respectively.

Figure 16 illustrates the energy levels of the ground and first excited states as a function of ϕ_F for a given electric field $F = 1F^*$. We provide several calculations keeping the radius of the curved surface constant to R = 15.9, 23.9 and 47.7 nm, respectively, with varying ϕ_F from 0° to 180°. The width is fixed to W = 75 nm.

Increasing ϕ_F causes the energy levels gradually decrease for all radius values, and it impacts significantly when the surface is less curved (R = 47.7 nm). For the first excited state, ϕ_F less than 45° can push the energy levels to the peak values before slowly declining to the lowest points.
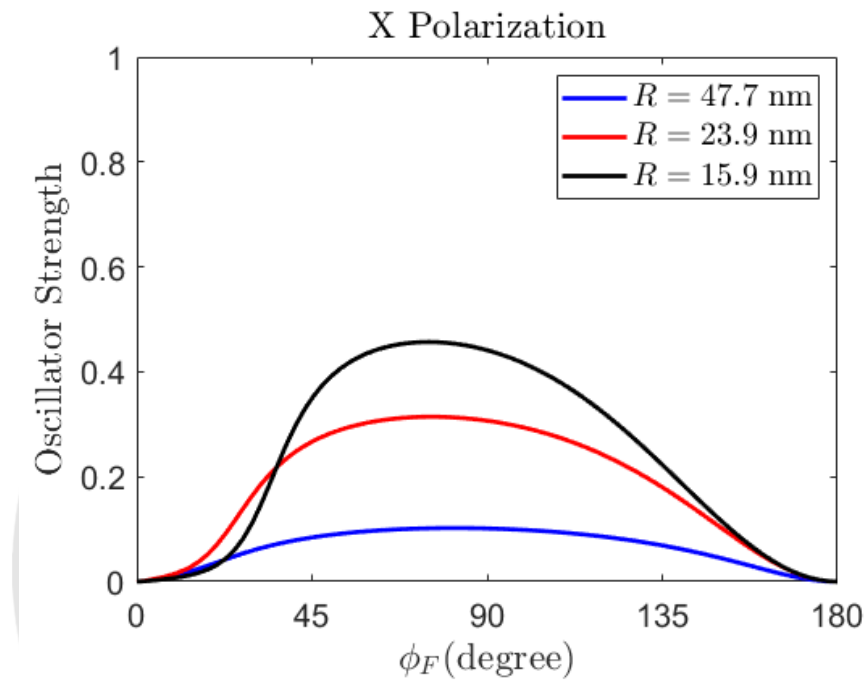
Figure 17. The oscillator strength along the x-direction between the ground and first excited states as a function of ϕ_F with R = 15.9, 23.9 and 47.7 nm, respectively.
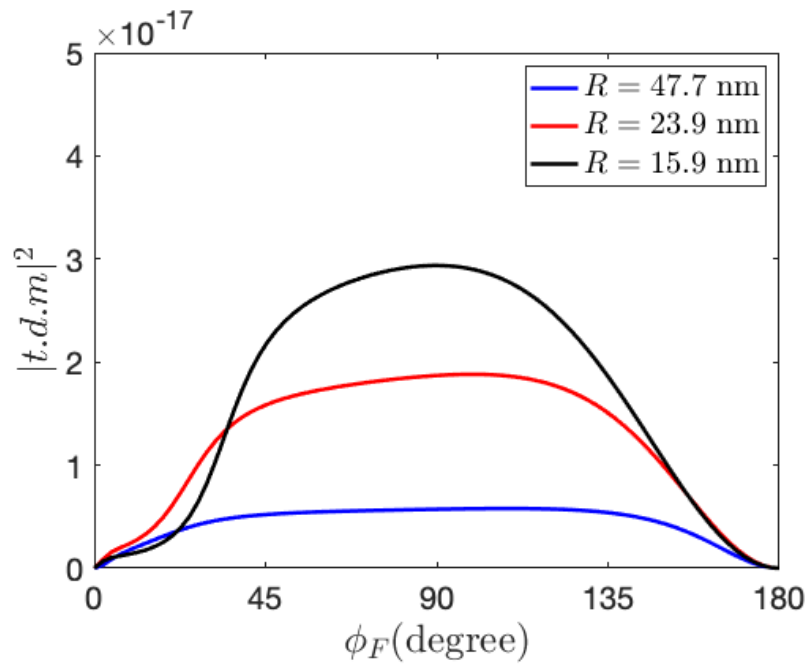
Figure 18. The transition dipole moment (t.d.m.) squared of the oscillator strength corresponds to Figure 17 as a function of ϕ_F with R = 15.9, 23.9 and 47.7 nm, respectively.

We previously knew that the oscillator strength between the ground and first excited states was almost zero when polarized light in the x-direction interacted with a curved surface. However, the electric field with varying ϕ_F can enhance the oscillator strength in that case. Figure 17 illustrates the oscillator strength along the x-direction between the ground and first excited states as a function of ϕ_F for a given electric field $F = 1F^*$ and various radius values. Figure 18 demonstrates the transition dipole moment squared of the oscillator strength in Figure 17 as a function of ϕ_F. For all radius values, increasing ϕ_F drives the oscillator strength to the maximum points, which are higher when curvature is greater, then the oscillator strength declines to zero at ϕ_F = 180°. This result is because proper angle ϕ_F and curvature enhance the coupling between the ground and first excited states along the x-direction.
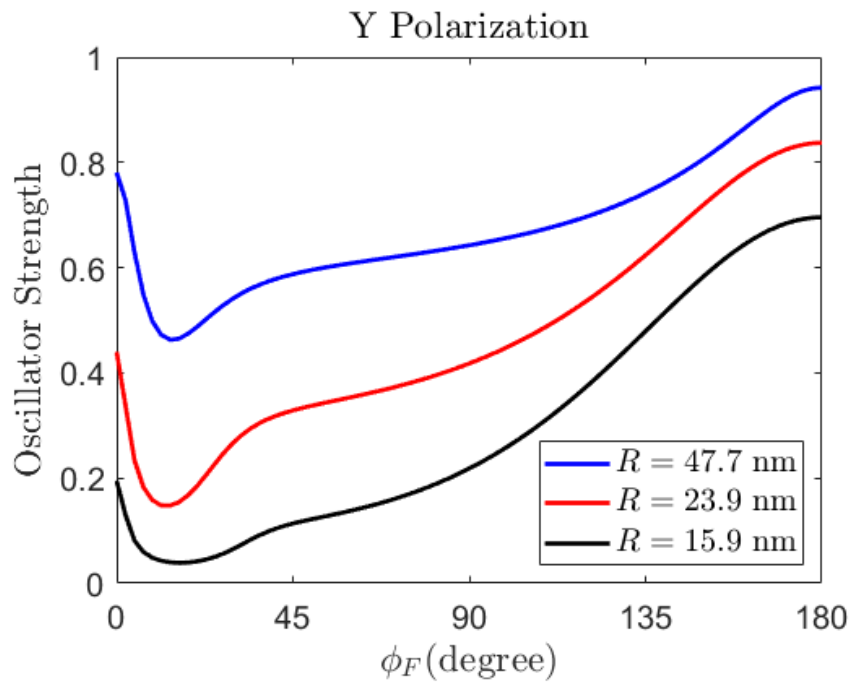
Figure 19. The oscillator strength along the y-direction between the ground and first excited states as a function of ϕ_F with R = 15.9, 23.9 and 47.7 nm, respectively.
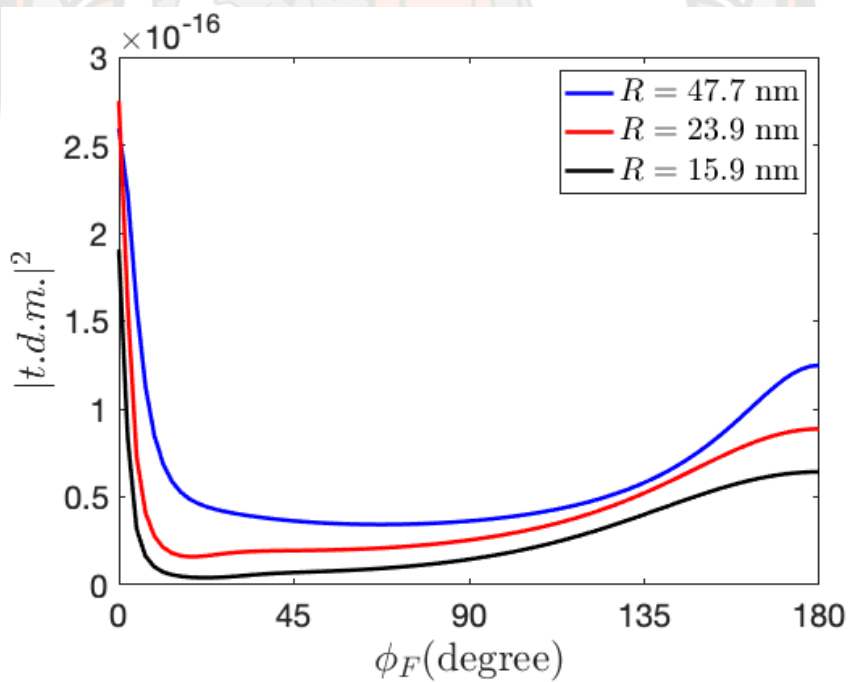
Figure 20. The transition dipole moment (t.d.m.) squared of the oscillator strength corresponds to Figure 19 as a function of ϕ_F with R = 15.9, 23.9 and 47.7 nm, respectively.

Figure 19 shows the oscillator strength along the y-direction between the ground and first excited states as a function of ϕ_F for a given electric field $F = 1F^*$ and various radius. Figure 20 demonstrates the transition dipole moment squared of the oscillator strength in Figure 19 as a function of ϕ_F. Overall, the curvature, increasing R, can shift the oscillator strength line lower. This result is different from the prior case since the curvature reduces the coupling between the ground and first excited states along the y-direction. In detail, increasing ϕ_F at the beginning lowers the oscillator strength to be minimum, then inclines monotonously to reach the maximum at ϕ_F = 180°. Those peaks are also higher than the value at ϕ_F = 0°. The reason for weak oscillator strength is that ϕ_F less than 15° is critical in eliminating the coupling between those states along the y-direction. The electric field along the -x-direction can considerably upgrade the sensitivity of y-polarized light.
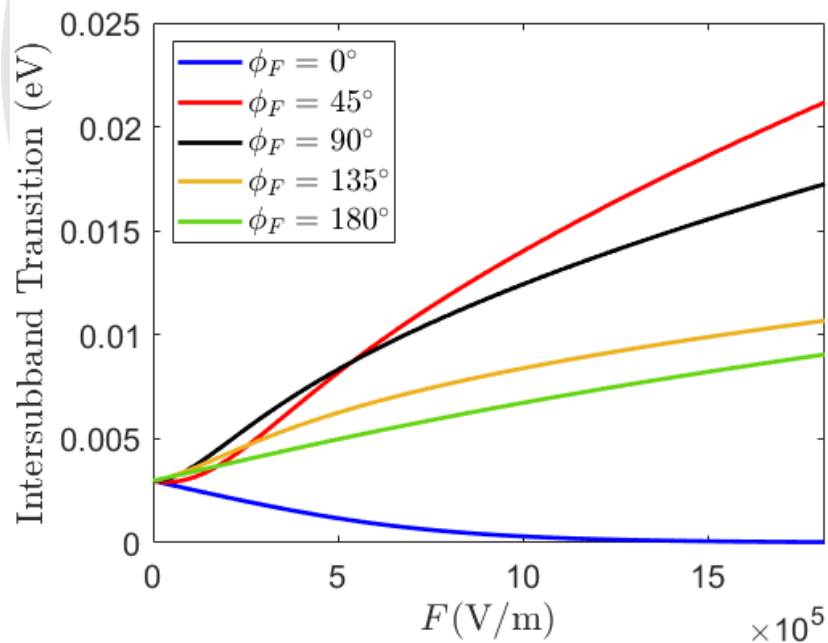
Figure 21. The intersubband transition energy between the ground and first excited states as a function of F with ϕ_F = 0°, 45°, 90°, 135° and 180°, respectively.
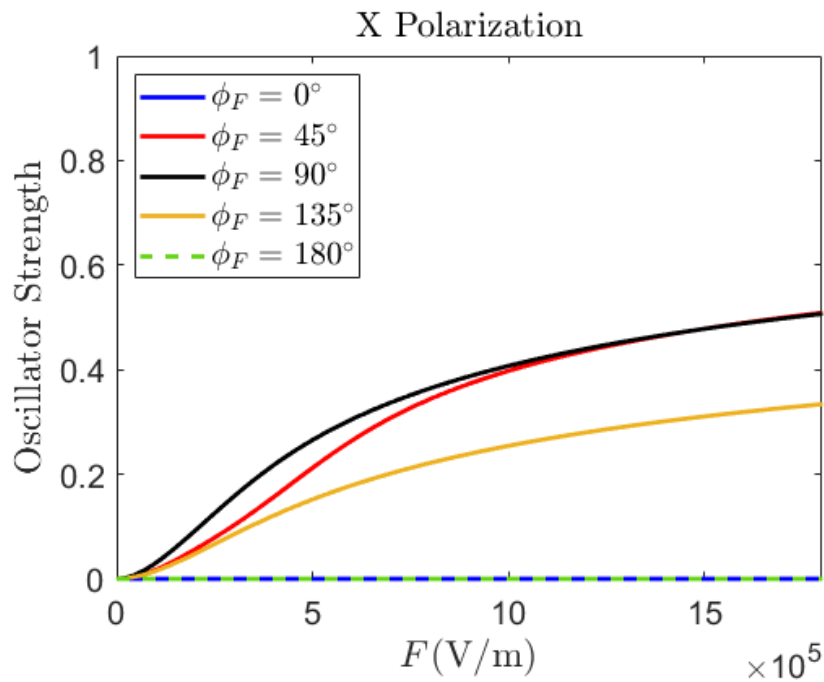
Figure 22. The oscillator strength along the x-direction between the ground and first excited states as a function of F with $\phi_F = 0°$, 45°, 90°, 135° and 180°, respectively.
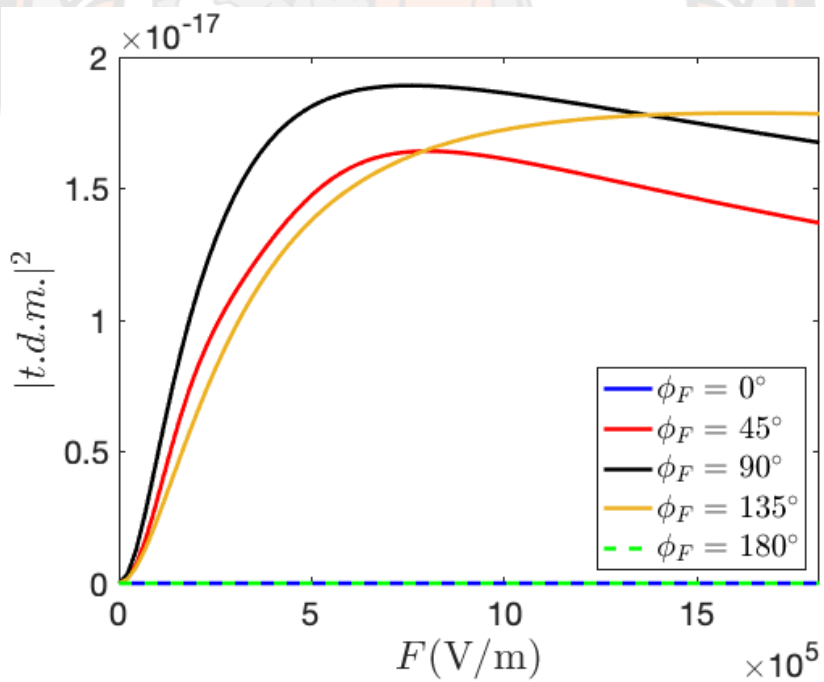
Figure 23. The transition dipole moment (t.d.m.) squared of the oscillator strength corresponds to Figure 22 as a function of F with $\phi_F = 0°$, 45°, 90°, 135° and 180°, respectively.

After we comprehend the curvature effect, the impact of the electric field magnitude is studied by choosing the curved surface with W = 75 nm and R = 23.9 nm. Figure 21 exhibits the intersubband transition energy between the ground and first excited states as a function of F with various ϕ_F. For $\phi_F = 0°$, increasing F gradually shrinks the intersubband transition energy, while others rapidly rise, precisely $\phi_F = 45°$ and 90°. Therefore, $\phi_F = 0°$ tends to diminish the oscillator strength, while tilt angles can strengthen the oscillator strength.

Figure 22 demonstrates the oscillator strength along the x-direction between the ground and first excited states as a function of F with various ϕ_F. Figure 23 demonstrates the transition dipole moment squared of the oscillator strength in Figure 22 as a function of F. The oscillator strength has zero value for all F when ϕ_F aligns on the x-axis ($\phi_F = 0°$ and 180°). Although the intersubband transition energy at $\phi_F = 180°$ supports the oscillator strength, F with $\phi_F = 180°$ annihilates the coupling between the two states along the x-direction. However, increasing F with tilt angles ϕ_F still continuously improves the oscillator strength along the x-direction.
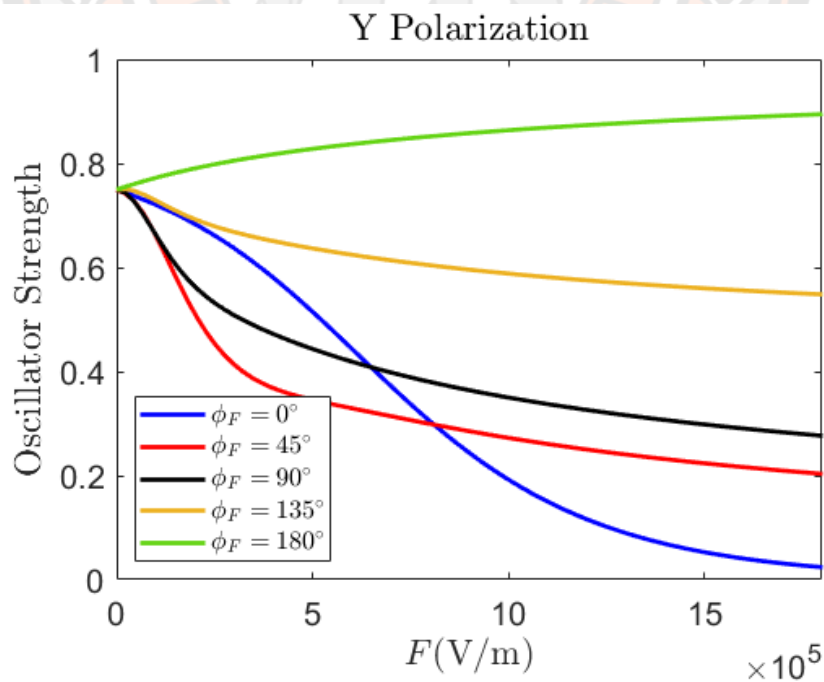
Figure 24. The oscillator strength along the y-direction between the ground and first excited states as a function of F with ϕ_F = 0°, 45°, 90°, 135° and 180°, respectively.
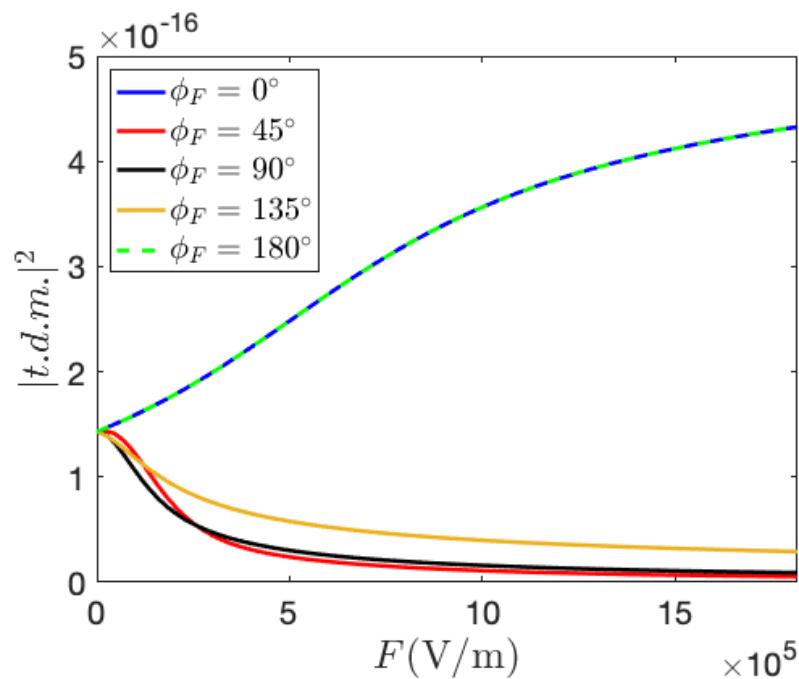
Figure 25. The transition dipole moment (t.d.m.) squared of the oscillator strength corresponds to Figure 24 as a function of F with ϕ_F = 0°, 45°, 90°, 135° and 180°, respectively.

Figure 24 shows the oscillator strength along the y-direction between the ground and first excited states as a function of F with various ϕ_F. Figure 25 demonstrates the transition dipole moment squared of the oscillator strength in Figure 24 as a function of F. Increasing F with various ϕ_F values reduces the oscillator strength. Interestingly, the decreasing pattern at ϕ_F = 0° is different from the others because the coupling between the ground and first excited states is great when the magnitude of an electric field is large. The result is a contrast to the intersubband transition energy; therefore, the oscillator strength plummets. Except for ϕ_F = 180°, the oscillator strength consistently enhances over F because those factors go in the same direction.

CHAPTER 5 CONCLUSIONS

In conclusion, we used a two-dimensional finite difference method to investigate rolled-up GaAs/AlGaAs layers with a constant radius in the presence of an electric field. On the binding energies, we present the coincidental effects of the radius of the curved surface, the donor position, the system's size, and the direction of an electric field. Without an electric field, the results indicate that the binding energies generated by an interior donor are more than those produced by an edge donor. When the radius value is smaller than the effective Bohr radius a^*, the displacement between a donor and an electron declines, resulting in a rapidly increase in the binding energies. Interestingly, the transition of electron distributions results in a substantial increase in the first excited state binding energy when a donor is on the right side of the wide surface. After adding an electric field, a complicated variation of the binding energies at each donor location happens. It can be comprehended and evaluated by observing the electron distributions without a donor. High binding energies occur when a donor is doped near the peak of electron distributions. Similarly, we believe that the binding energies in other structures can be anticipated using the location of the peak of probability and a donor impurity. On the oscillator strength, we report the impacts of the curved surface's radius, the surface's width, and the direction of an electric field. The study found that the lower radius value causes the weak oscillator strength along the y-direction because of the lower coupling between the ground and first excited states. An angle of an electric field can tune the oscillator strength. The tilt angle enhances the oscillator strength along the x-direction; however, that is eliminated when the electric field aligns on the x-axis. In the y-direction, the oscillator strength reduces at the beginning of increasing the angle value. Then, it increases monotonously to the maximum. The magnitude of an electric field improves the oscillator strength along the x-direction, but not when the angle is at $0°$ and $180°$. The result is the opposite for each angle in the y-direction. Except for the angle of $0°$, the oscillator strength is still weak over electric field strength because of the lower intersubband transition energy. From both studies, we expect them to be relevant for future research and can be applied to curved 2DES-based electrical products.

APPENDIX

A. The Hamiltonian for a particle constrained on a cylindrical surface

The Hamiltonian for a particle bound on a cylindrical surface is deduced in this section using the straightforward method described by Shikakhwa and Chair [57]. To begin, consider the case of a free particle in three-dimensional space. the system's Hamiltonian in cylindrical coordinates (ρ, ϕ, z) is

$$H_{3D} = -\frac{\hbar^2}{2\mu}\left(\frac{1}{\rho}\frac{\partial}{\partial\rho}\left(\rho\frac{\partial}{\partial\rho}\right) + \frac{1}{\rho^2}\frac{\partial^2}{\partial\phi^2} + \frac{\partial^2}{\partial z^2}\right). \tag{6.1}$$

When a radial momentum operator $\hat{p}_\rho = -i\hbar\left(\frac{\partial}{\partial\rho} + \frac{1}{2\rho}\right)$ is defined. The Hamiltonian can be expressed as

$$H_{3D} = \frac{p_\rho^2}{2\mu} - \frac{\hbar^2}{2\mu}\left(\frac{1}{\rho^2}\frac{\partial^2}{\partial\phi^2} + \frac{\partial^2}{\partial z^2}\right) - \frac{\hbar^2}{8\mu\rho^2}. \tag{6.2}$$

If a strong radial potential $V(\rho)$ is provided into the system, it can be assumed that a particle is confined on a cylindrical surface. Consequently, the radial momentum can be ignored, and R, the radius of the surface, can be substituted for the coordinate ρ. At this point, the system is two-dimensional, and Hamiltonian is

$$H_{2D} = -\frac{\hbar^2}{2\mu}\left(\frac{1}{R^2}\frac{\partial^2}{\partial\phi^2} + \frac{\partial^2}{\partial z^2}\right) - \frac{\hbar^2}{8\mu R^2}. \tag{6.3}$$

Normally, the second term is referred to as the geometric potential [31, 32], which is obtained from the curvature of a cylindrical surface. Additionally, Ortix et al. enhanced the Hamiltonian for a curved multilayer nanostructure [58]. Strain in curved layers creates another geometric potential for conduction electrons due to the model-solid theory [59]. The authors demonstrate that the formula of the geometric potential due to strain, derived from the adiabatic separation approach, is identical to that of the geometric potential. As a result, the Hamiltonian becomes

$$H_{2D} = -\frac{\hbar^2}{2\mu}\left(\frac{1}{R^2}\frac{\partial^2}{\partial\phi^2} + \frac{\partial^2}{\partial z^2}\right) - \frac{\upsilon_R\hbar^2}{8\mu R^2}, \tag{6.4}$$

where υ_R is the parameter that indicates the geometric potential strength affected by both the curvature and strain.

B. Two-dimensional electron system on a curved surface with a constant radius

In this section, we will show how to solve equation (3.4). That equation is separable differential equation; therefore, the eigenstate is assumed as

$$\Psi(\phi, z) = \Phi(\phi)Z(z) \tag{6.5}$$

Substituting equation (6.5) into equation (3.4), it becomes

$$-\frac{\hbar^2}{2\mu R^2}\Phi''(\phi)Z(z) - \frac{\hbar^2}{2\mu}\Phi(\phi)Z''(z) = \left(E_0 + \frac{\upsilon_R\hbar^2}{8\mu R^2}\right)\Phi(\phi)Z(z). \tag{6.6}$$

Equation (6.6) is divided by $\Phi(\phi)Z(z)$, it will be obtained

$$-\frac{\hbar^2}{2\mu R^2}\frac{\Phi''(\phi)}{\Phi(\phi)} - \frac{\hbar^2}{2\mu}\frac{Z''(z)}{Z(z)} = E_0 + \frac{\upsilon_R\hbar^2}{8\mu R^2}. \tag{6.7}$$

Equation (6.7) can be separated into two independent expressions as

$$-\frac{\hbar^2}{2\mu R^2}\Phi''(\phi) = \varepsilon_\phi\Phi(\phi) \tag{6.8}$$

and

$$-\frac{\hbar^2}{2\mu}Z''(z) = \varepsilon_z Z(z). \tag{6.9}$$

ε_ϕ and ε_z are the energies which depend on the ϕ-axis and z-axis, respectively. Form equations (6.7), (6.8) and (6.9), total energy E of the system is

$$E = \varepsilon_\phi + \varepsilon_z - \frac{\upsilon_R\hbar^2}{8\mu R^2}. \tag{6.10}$$

The general solutions of equations (6.8) and (6.9) are

$$\Phi(\phi) = A_\phi \sin(k_\phi\phi) + B_\phi \cos(k_\phi\phi) \tag{6.11}$$

and

$$Z(z) = A_z \sin(k_z z) + B_z \cos(k_z z) \tag{6.12}$$

which A_ϕ, B_ϕ, A_z and B_z are constants from a normalization. k_ϕ and k_z are defined as $k_\phi = \sqrt{\dfrac{2\mu R^2\varepsilon_\phi}{\hbar^2}}$ and $k_z = \sqrt{\dfrac{2\mu\varepsilon_z}{\hbar^2}}$, respectively. The boundary conditions of the curved surface are $\Phi(\phi_{\min}) = \Phi(\phi_{\max}) = 0$ and $Z(z_{\min}) = Z(z_{\max}) = 0$, then equations (6.11) and (6.12) can be rewritten with such conditions as

$$0 = A_\phi \sin(k_\phi\phi_{\min}) + B_\phi \cos(k_\phi\phi_{\min}), \tag{6.13}$$

$$0 = A_\phi \sin(k_\phi\phi_{\max}) + B_\phi \cos(k_\phi\phi_{\max}), \tag{6.14}$$

$$0 = A_z \sin(k_z z_{\min}) + B_z \cos(k_z z_{\min}), \tag{6.15}$$

and

$$0 = A_z \sin(k_z z_{\max}) + B_z \cos(k_z z_{\max}). \tag{6.16}$$

From equation (6.13), it will be obtained

$$B_\phi = -A_\phi \tan(k_\phi \phi_{\min}) \tag{6.17}$$

Substituting equation (6.17) into equation (6.14), the relation between $k_\phi \phi_{\min}$ and $k_\phi \phi_{\max}$ is $\tan(k_\phi \phi_{\max}) = \tan(k_\phi \phi_{\min})$. Therefore, it is found that $k_\phi (\phi_{\max} - \phi_{\min}) = n_\phi \pi$ which n_ϕ is a positive integer. Form the definition of k_ϕ, the energy ε_ϕ along the ϕ-axis is

$$\varepsilon_\phi = \frac{n_\phi^2 \pi^2 \hbar^2}{2\mu W^2} \tag{6.18}$$

which the width W of the curved surface is equal to $R(\phi_{\max} - \phi_{\min})$. When the same method is used in equation (6.15) and (6.16), this gives the result,

$$\varepsilon_z = \frac{n_z^2 \pi^2 \hbar^2}{2\mu L^2}. \tag{6.19}$$

n_z is a positive integer, and the length L of the curved surface is equal to $z_{\max} - z_{\min}$. Eventually, the energy level of the curved surface with a constant radius is

$$E_0 = \frac{n_\phi^2 \pi^2 \hbar^2}{2\mu W^2} + \frac{n_z^2 \pi^2 \hbar^2}{2\mu L^2} - \frac{\upsilon_R \hbar^2}{8\mu R^2} \tag{6.20}$$

For the exact solution of a wavefunction, the identity of trigonometry can be used:

$$N_\phi \sin(k_\phi \phi + \alpha_\phi) = N_\phi \cos\alpha_\phi \sin(k_\phi \phi) + N_\phi \sin\alpha_\phi \cos(k_\phi \phi). \tag{6.21}$$

N_ϕ and α_ϕ are the arbitrary constant and the phase angle, respectively. When equation (6.11) is compared to equation (6.21), it is found that $A_\phi = N_\phi \cos\alpha_\phi$ and $B_\phi = N_\phi \sin\alpha_\phi$. From both expressions, the relation of N_ϕ, α_ϕ, A_ϕ and B_ϕ is obtained:

$$N_\phi = \sqrt{A_\phi^2 + B_\phi^2} \tag{6.22}$$

and

$$\tan\alpha_\phi = \frac{B_\phi}{A_\phi} \tag{6.23}$$

Therefore, equation (6.11) and (6.12), used the following implementation, can be rewritten as

$$\Phi(\phi) = N_\phi \sin\left(\frac{n_\phi \pi R \phi}{W} + \alpha_\phi\right), \tag{6.24}$$

and

$$Z(z) = N_z \sin\left(\frac{n_z \pi z}{L} + \alpha_z \right). \tag{6.25}$$

N_z and α_z are the arbitrary constant and the phase angle, respectively. Then, α_ϕ and α_z have to be solved by using the boundary condition of the curved surface $\Phi(\phi_{max}) = 0$ and $Z(z_{max}) = 0$:

$$0 = N_\phi \sin\left(\frac{n_\phi \pi R \phi_{max}}{W} + \alpha_\phi \right), \tag{6.26}$$

and

$$0 = N_z \sin\left(\frac{n_z \pi z_{max}}{L} + \alpha_z \right). \tag{6.27}$$

From equation (6.26) and (6.27), the solution of α_ϕ and α_z are $-\dfrac{n_\phi \pi R \phi_{min}}{W}$ and $-\dfrac{n_z \pi z_{min}}{L}$, respectively, and substitute the results into those expressions. Therefore, the exact solution of a wavefunction in equation (6.5) becomes

$$\Psi(\phi, z) = N \sin\left(\frac{n_\phi \pi R}{W}(\phi - \phi_{min}) \right) \sin\left(\frac{n_z \pi}{L}(z - z_{min}) \right). \tag{6.28}$$

N_ϕ and N_z can be combined to a constant N. Lastly, the value of N is obtained from the normalized condition:

$$\int_{z_{min}}^{z_{max}} \int_{\phi_{min}}^{\phi_{max}} |\Psi(\phi, z)|^2 R d\phi dz = 1$$

$$\int_{z_{min}}^{z_{max}} \int_{\phi_{min}}^{\phi_{max}} N^2 \sin^2\left(\frac{n_\phi \pi R}{W}(\phi - \phi_{min}) \right) \sin^2\left(\frac{n_z \pi}{L}(z - z_{min}) \right) R d\phi dz = 1$$

$$N^2 \int_{\phi_{min}}^{\phi_{max}} \sin^2\left(\frac{n_\phi \pi R}{W}(\phi - \phi_{min}) \right) R d\phi \int_{z_{min}}^{z_{max}} \sin^2\left(\frac{n_z \pi}{L}(z - z_{min}) \right) dz = 1 \tag{6.29}$$

$$N^2 \cdot \frac{W}{2} \cdot \frac{L}{2} = 1$$

$$N = \frac{2}{\sqrt{WL}}.$$

Substituting N into equation (6.28), the complete exact solution of a wavefunction is

$$\Psi(\phi, z) = \frac{2}{\sqrt{WL}} \sin\left(\frac{n_\phi \pi R}{W}(\phi - \phi_{min}) \right) \sin\left(\frac{n_z \pi}{L}(z - z_{min}) \right). \tag{6.30}$$

REFERENCES

1. Moraru, D., et al., *Atom devices based on single dopants in silicon nanostructures.* Nanoscale research letters, 2011. **6**(1): p. 1-9.

2. Shinada, T., et al., *Enhancing semiconductor device performance using ordered dopant arrays.* Nature, 2005. **437**(7062): p. 1128-1131.

3. Lansbergen, G., et al., *Gate-induced quantum-confinement transition of a single dopant atom in a silicon FinFET.* Nature Physics, 2008. **4**(8): p. 656-661.

4. Rahman, R., et al., *Orbital Stark effect and quantum confinement transition of donors in silicon.* Physical Review B, 2009. **80**(16): p. 165314.

5. Hollenberg, L., et al., *Charge-based quantum computing using single donors in semiconductors.* Physical Review B, 2004. **69**(11): p. 113301.

6. Wang, Y., et al., *Highly tunable exchange in donor qubits in silicon.* npj Quantum Information, 2016. **2**: p. 16008.

7. Pla, J.J., et al., *A single-atom electron spin qubit in silicon.* Nature, 2012. **489**(7417): p. 541.

8. Pawlis, A., et al., *Lasing of donor-bound excitons in ZnSe microdisks.* Physical Review B, 2008. **77**(15): p. 153304.

9. Holovatsky, V., O. Voitsekhivska, and M.Y. Yakhnevych, *The effect of magnetic field and donor impurity on electron spectrum in spherical core-shell quantum dot.* Superlattices and Microstructures, 2018. **116**: p. 9-16.

10. Zouitine, A., et al., *Spatial separation effect on the energies of uncorrelated and correlated electron-hole pair in CdSe/ZnS and InAs/InP core/shell spherical quantum dots.* Superlattices and Microstructures, 2017. **109**: p. 123-133.

11. Peter, A.J., *Hydrogenic impurities in cylindrical quantum wires in the presence of a magnetic field.* Physica E: Low-dimensional Systems and Nanostructures, 2007. **39**(1): p. 115-119.

12. Tshipa, M., et al., *Donor impurity binding energies of coaxial GaAs/AlxGa1−xAs cylindrical quantum wires in a parallel applied magnetic field.* Superlattices and

Microstructures, 2018. **116**: p. 227-237.

13. Kalpana, P.S. and K. Jayakumar, *Helium like impurity in CdTe/Cd1-xMnxTe semimagnetic semiconductors under magnetic field: Dimensionality effect on electron–Electron interaction.* Superlattices and Microstructures, 2017. **111**: p. 115-122.

14. Akbas, H., et al., *The effect of magnetic field in a GaAs/AlAs spherical quantum dot with a hydrogenic impurity.* Physica E: Low-dimensional Systems and Nanostructures, 2009. **41**(4): p. 605-608.

15. Boz, F.K., et al., *Energy levels of GaAs/AlxGa1-xAs/AlAs spherical quantum dot with an impurity.* Applied Surface Science, 2016. **387**: p. 76-81.

16. Chafai, A., et al., *Tuning the binding energy of on-center donor in CdSe/ZnTe core/shell quantum dot by spatial parameters and magnetic field strength.* Physica E: Low-dimensional Systems and Nanostructures, 2017. **94**: p. 96-99.

17. Chafai, A., et al., *Hydrogenic donor in a CdSe/CdS quantum dot: Effect of electric field strength, nanodot shape and dielectric environment on the energy spectrum.* Physica E: Low-dimensional Systems and Nanostructures, 2018. **104**: p. 29-35.

18. Boz, F., et al., *The multilayered spherical quantum dot under a magnetic field.* Applied Surface Science, 2010. **256**(12): p. 3832-3836.

19. Aktas, S., F.K. Boz, and S.S. Dalgic, *Electric and magnetic field effects on the binding energy of a hydrogenic donor impurity in a coaxial quantum well wire.* Physica E: Low-dimensional Systems and Nanostructures, 2005. **28**(1): p. 96-105.

20. Tangarife, E. and C. Duque, *Combined effects of hydrostatic pressure and electric field on the donor binding energy and polarizability in laterally coupled double InAs/GaAs quantum-well wires.* Applied Surface Science, 2010. **256**(23): p. 7234-7241.

21. Boz, F.K. and S. Aktas, *Magnetic field effect on the binding energy of a hydrogenic impurity in coaxial GaAs/AlxGa1− xAs quantum well wires.* Superlattices and Microstructures, 2005. **37**(4): p. 281-291.

22. Kes, H., et al., *Binding energy of a hydrogenic impurity in a coaxial quantum wire*

with an insulator layer. Superlattices and Microstructures, 2017. **111**: p. 966-975.

23. Hu, M., et al., *Comparison of external electric and magnetic fields effect on binding energy of hydrogenic donor impurity in different shaped quantum wells.* The European Physical Journal B, 2018. **91**(1): p. 19.

24. Kalpana, P.S., P. Nithiananthi, and K. Jayakumar, *Donor states in a semimagnetic Cd1━ xinMnxinTe/Cd1━ xoutMnxoutTe Double Quantum Well.* Superlattices and Microstructures, 2017. **102**: p. 246-258.

25. Vartanian, A., et al., *Influence of image charge effect on the binding energy of hydrogen-like donor impurity in a near-surface quantum well under transverse electric field.* Physica E: Low-dimensional Systems and Nanostructures, 2019. **106**: p. 1-4.

26. Viri, D. and R. Del Sole, *Exact solution of the Schrödinger equation for Wannier excitons on a microsphere.* Solid state communications, 1996. **97**(11): p. 985-989.

27. Kayanuma, Y. and N. Saito, *Wannier excitons on a microsphere.* Solid state communications, 1992. **84**(7): p. 771-774.

28. Malachias, A., et al., *Direct strain and elastic energy evaluation in rolled-up semiconductor tubes by x-ray microdiffraction.* Physical Review B, 2009. **79**(3): p. 035301.

29. Costescu, R.M., et al., *Rolled-up nanotech: illumination-controlled hydrofluoric acid etching of AlAs sacrificial layers.* Nanoscale research letters, 2009. **4**(12): p. 1463.

30. Mendach, S., et al., *Preparation of curved two-dimensional electron systems in InGaAs/GaAs-microtubes.* Physica E: Low-dimensional Systems and Nanostructures, 2004. **23**(3-4): p. 274-279.

31. Chang, C.-H., J. Van Den Brink, and C. Ortix, *Strongly anisotropic ballistic magnetoresistance in compact three-dimensional semiconducting nanoarchitectures.* Physical review letters, 2014. **113**(22): p. 227205.

32. Ortix, C. and J. van den Brink, *Effect of curvature on the electronic structure and bound-state formation in rolled-up nanotubes.* Physical Review B, 2010. **81**(16): p.

165419.

33.   Prinz, V.Y., et al., *Free-standing and overgrown InGaAs/GaAs nanotubes, nanohelices and their arrays.* Physica E: Low-dimensional Systems and Nanostructures, 2000. **6**(1-4): p. 828-831.

34.   Songmuang, R., et al., *Si O x⁄ Si radial superlattices and microtube optical ring resonators.* Applied Physics Letters, 2007. **90**(9): p. 091905.

35.   Kipp, T., et al., *Optical modes in semiconductor microtube ring resonators.* Physical review letters, 2006. **96**(7): p. 077403.

36.   Bernardi, A., et al., *On-chip Si/SiO x microtube refractometer.* Applied Physics Letters, 2008. **93**(9): p. 094106.

37.   Thurmer, D.J., et al., *Process integration of microtubes for fluidic applications.* Applied physics letters, 2006. **89**(22): p. 223507.

38.   Grimm, D., et al., *Rolled-up nanomembranes as compact 3D architectures for field effect transistors and fluidic sensing applications.* Nano letters, 2012. **13**(1): p. 213-218.

39.   Demtröder, W., *Laser spectroscopy.* Vol. 2. 1982: Springer.

40.   Robinson, J.W., *Atomic spectroscopy.* 1996: CRC Press.

41.   Wu, S., et al., *Tuning of the intersubband absorption in a shallow InAs/InP quantum wire by a transverse electric field.* Superlattices and Microstructures, 2014. **67**: p. 33-39.

42.   Özmen, A., et al., *Computation of the oscillator strength and absorption coefficients for the intersubband transitions of the spherical quantum dot.* Optics Communications, 2009. **282**(19): p. 3999-4004.

43.   Mendach, S., et al., *Evenly curved two-dimensional electron systems in rolled-up Hall bars.* Applied physics letters, 2006. **88**(21): p. 212113.

44.   Vorob'ev, A., et al., *Magnetotransport properties of two-dimensional electron gas on cylindrical surface.* Physica E: Low-dimensional Systems and Nanostructures, 2004. **23**(1-2): p. 171-176.

45.   Yang, X., et al., *Analytic solution of a two-dimensional hydrogen atom. I.*

Nonrelativistic theory. Physical Review A, 1991. **43**(3): p. 1186.

46.   Parfitt, D.G. and M.E. Portnoi, *The two-dimensional hydrogen atom revisited.* Journal of Mathematical Physics, 2002. **43**(10): p. 4681-4691.

47.   Galbiati, N., et al., *Investigation of Si as an n-type dopant in AlGaAs grown by molecular beam epitaxy on high index planes.* Semiconductor science and technology, 1997. **12**(5): p. 555.

48.   Galbiati, N., et al., *Photoluminescence investigation of Si as p-type dopant in AlGaAs grown by molecular beam epitaxy on high-index planes.* Semiconductor science and technology, 1996. **11**(12): p. 1830.

49.   Hwang, E. and S.D. Sarma, *Limit to two-dimensional mobility in modulation-doped GaAs quantum structures: How to achieve a mobility of 100 million.* Physical Review B, 2008. **77**(23): p. 235437.

50.   Kane, M., et al., *Parallel conduction in GaAs/AlxGa1-xAs modulation doped heterojunctions.* Journal of Physics C: Solid State Physics, 1985. **18**(29): p. 5629.

51.   Solomon, P.M. and H. Morkoc, *Modulation-doped GaAs/AlGaAs heterojunction field-effect transistors (MODFET's), ultrahigh-speed device for supercomputers.* IEEE Transactions on Electron Devices, 1984. **31**(8): p. 1015-1027.

52.   Nguyen, L.D., L.E. Larson, and U.K. Mishra, *Ultra-high speed modulation-doped field-effect transistors: a tutorial review.* Proceedings of the IEEE, 1992. **80**(4): p. 494-518.

53.   Huebener, R., *Conductors, semiconductors, superconductors. An introduction to solid-state physics. For physicists, engineers, and natural scientists.* 2013.

54.   Arfken, G., *Confluent hypergeometric functions.* Mathematical Methods for Physicists, 1985: p. 753-758.

55.   Roman, S., *The umbral calculus.* 2005: Springer.

56.   Pramjorn, N. and A. Amthong, *Donor binding energies in a curved two-dimensional electron system.* Applied Surface Science, 2020. **508**: p. 145195.

57.   Shikakhwa, M., *Hermitian and gauge-covariant Hamiltonians for a particle in a magnetic field on cylindrical and spherical surfaces.* European Journal of Physics,

2016. **38**(1): p. 015402.

58.   Ortix, C., et al., *Curvature-induced geometric potential in strain-driven nanostructures.* Physical Review B, 2011. **84**(4): p. 045438.

59.   Van de Walle, C.G., *Band lineups and deformation potentials in the model-solid theory.* Physical review B, 1989. **39**(3): p. 1871.